Research Article

ADVANCED PHOTONICS

Light control of lasing from liquid-crystal micro-droplet light switch

Vandna Sharma,[a,b,†] **Jaka Zaplotnik**,[a,c,†] **Maruša Mur**,[a,†] **Jaka Pišljar**,[a,c,†] **Uroš Jagodič**,[a] **Andreja Jelen**,[a] **Miha Škarabot**,[a,c] **Urban Mur**,[c,d] **Miha Ravnik**,[a,c] **and Igor Muševič**[a,c,*]
[a]Jožef Stefan Institute, Condensed Matter Physics Department, Ljubljana, Slovenia
[b]Chitkara University, Chitkara University Institute of Engineering and Technology, Centre for Liquid Crystal Research, Patiala, Punjab, India
[c]University of Ljubljana, Faculty of Mathematics and Physics, Ljubljana, Slovenia
[d]University of Oxford, Department of Engineering Science, Oxford, United Kingdom

Abstract. The all-optical control of light has been explored in hard matter, but to control light by light in soft matter is a major experimental and conceptual challenge that remains largely unexplored. We propose and verify experimentally and numerically that nanosecond light pulses can be controlled by light pulses using resonant stimulated-emission depletion (STED) in a liquid-crystal optical cavity that acts as a nanosecond optical switch. This light-by-light control is realized in a micrometer-diameter droplet of fluorescent-dye-doped nematic liquid crystal that is submersed in an aqueous solution. A set of laser-printed optical waveguides touches the surface of the droplet and provides flow of light in and out of the droplet. We demonstrate that nanosecond light pulses launched through the waveguides initiate the lasing of whispering gallery modes in the droplet. However, the lasing can be suppressed very efficiently on a nanosecond scale by another, red-shifted light pulse before the lasing takes place. The proposed concept of light control in soft matter using STED in an optical cavity requires fewer production steps because of self-assembly. It could be massively replicated using soft imprint lithography, uses less production energy due to low production temperatures, requires less toxic materials, and could be made entirely biocompatible and flexible.

Keywords: liquid crystals; lasing; whispering gallery modes; light control; stimulated-emission depletion.

Received Apr. 10, 2025; revised manuscript received Dec. 1, 2025; accepted for publication Feb. 2, 2026; published online Mar. 4, 2026.

[DOI: 10.1117/1.AP.8.2.026009]

1 Introduction

Soft-matter photonics[1] is an emerging field that is exploring the self-organization phenomena in soft matter to design and fabricate functional photonic devices. The interest in soft-matter photonics coincides with the foundation of the concept of a photonic crystal by Gmitter and Yablonovich in 1989[2] and the exploration of structural coloration in living organisms.[3–5] In parallel with the exploration of biomimetic photonic structures and materials, the concepts of the switching of light signals in soft matter were extensively explored. Because soft matter is not a very good conductor of electric signals, soft-matter photonic devices are envisaged to modulate optical signals exclusively by using light, which makes soft-matter photonics an inherently all-optical photonic platform.

Switching light by light in soft matter has primarily been achieved by modulating the index of refraction of optical cavities or coupling gap material via nonlinear optical phenomena induced by intense light pulses. Because the eigenfrequencies of an optical cavity depend on its index of refraction, the cavity can be tuned in or detuned-off-resonance with external modes, thus switching on and off the energy transfer between the cavity and environment.[6] Although all-optical modulation has been demonstrated in a number of studies on hard matter, particularly silicon,[7–11] the experimental demonstration of all-optical control in soft-matter photonics is scarce. By taking advantage of the highly nonlinear Kerr effect in polymers, red-

---

*Address all correspondence to Igor Muševič, igor.musevic@ijs.si

†These authors contributed equally to this work.

shifting of the defect mode frequency in 1D or 2D polymer photonic crystals results in ~1 to 10 ps switching times using moderate ~MW/cm^2 pump intensities of modulating light.[12–14] The corresponding single light-pulse energy to switch the light by light is 0.5 to 5 pJ.

Here, we demonstrate, both experimentally and numerically an alternative, soft matter approach to manipulating and switching light by light using stimulated-emission depletion (STED) in a resonant cavity.[15–17] In contrast to the lithographic structuring of organic thin films that are usually used to fabricate photonic cavities, we use a droplet of a nematic liquid crystal (LC) doped with a fluorescent dye as a whispering gallery mode (WGM) resonant cavity.[18–22] The concept of all-optical switching in a spherical LC micro-cavity is presented in Fig. 1. We use a two-photon 3D lithography to print four polymer tapered waveguides standing upright on a glass slide [Fig. 1(a)], and an LC droplet with some fluorescent dye is inflated in the middle of the waveguides (Video S1), touching the waveguides.

A laser pulse with the wavelength close to the maximum of the absorption spectrum of the dye is sent through a waveguide. This light is very efficiently coupled to the droplet, which emits short laser pulses, as shown in Fig. 1(a), with the emission spectrum showing very narrow WGM resonances.[14] However, this laser emission can be depleted by sending another laser pulse through the same waveguide before the lasing takes place, as illustrated in Fig. 1(b). This STED light pulse is resonantly

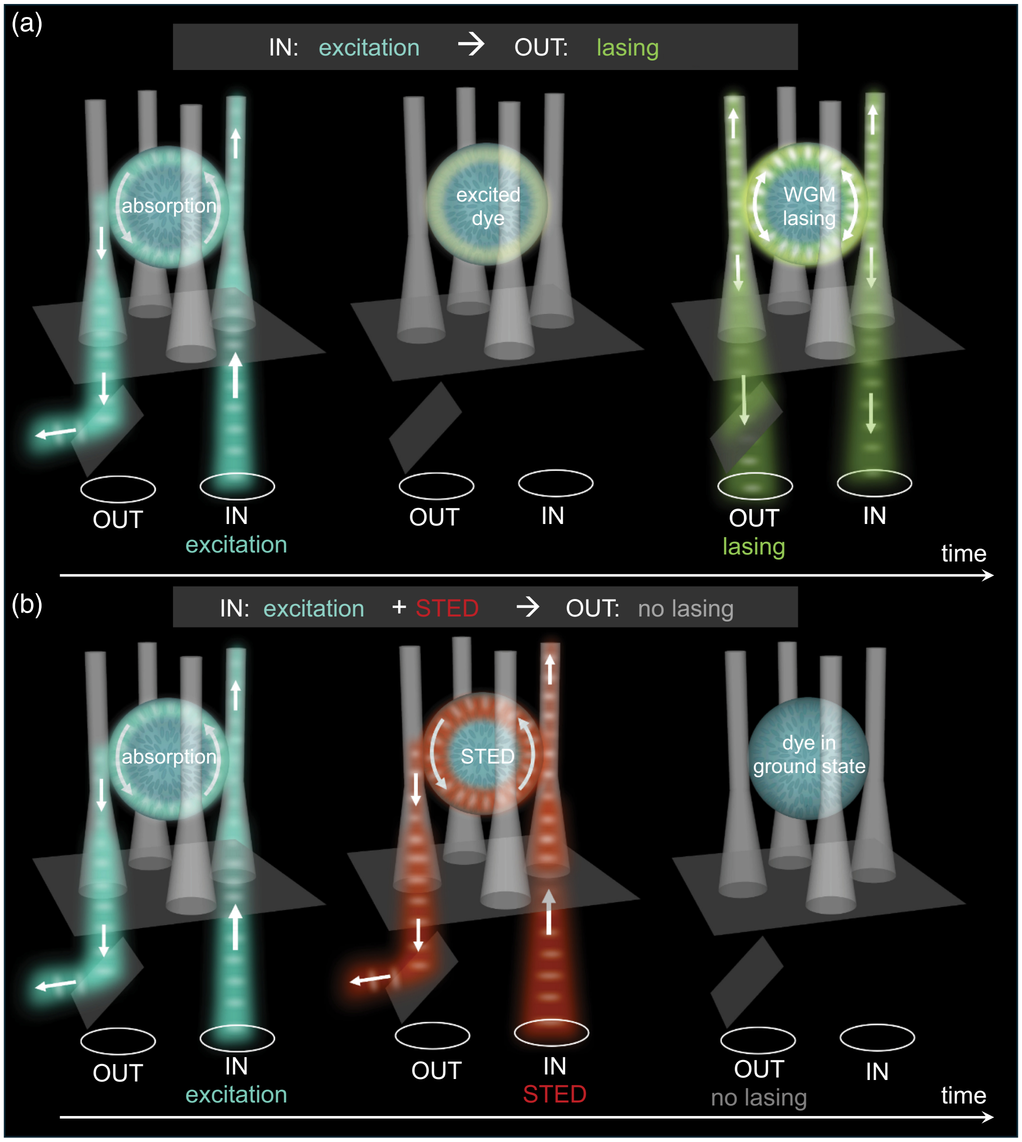

Fig. 1 Switching light by light in a dye-doped LC droplet: a WGM light switch. (a) After the cavity is excited with 532-nm pulse (blue bullets), the cavity starts lasing and emits WGMs into the waveguides (green bullets). (b) If STED pulse (red bullets) is sent into the cavity before the lasing takes place, the STED pulse will be amplified, while lasing will be depleted. The energy stored in excited dye molecules is resonantly transferred to the STED beam via stimulated emission. No lasing takes place, and STED beam is amplified. This changes the wavelength of the emitted light from green in (a) to red in (b).

amplified while circulating in the cavity, consuming the stored energy through the process of stimulated emission [Fig. 1(b)]. As a result, the amplified STED pulse is emitted, whereas the WGM lasing is depleted. This makes it possible to modulate and control the WGM lasing by light only.

The proposed novel soft matter approach is inherently three-dimensional and uses novel concepts of self-assembly of photonic microstructures in 3D, based on surface tension, designing and fabricating 3D polymer scaffolds to host soft matter photonic elements. This approach has important advantages over the traditional photonic technologies. First, it requires less production steps, as some crucial photonic elements, such as WGM spherical cavities, can be assembled in a fraction of a second compared with tens of production steps using hard matter. In fact, such 3D structures are difficult to produce using hard matter technology. Second, complex photonic circuits integrating waveguides and polymer scaffolds that host the soft matter active elements could be replicated using large-area soft imprint lithography. Last, but not least, soft-matter-based photonic structures are produced at low temperatures, require nontoxic materials, and could be made entirely biocompatible and flexible.

2 Materials and Methods

A set of five different nematic liquid crystals, MLC-2132, E7, 5CB, XV902-A00, and HNG7172-00-000, was used to perform the experiments. A detailed set of LC properties is listed in Table 1. A 1% (mass fraction) fluorescent dye (PM580) solution in acetone was prepared and mixed well to ensure all the dye was dissolved. To prepare the 0.2% (mass fraction) dye-doped liquid crystal mixtures, a known amount of the prepared acetone-dye solution was mixed with the LC and mixed using a vortex mixer. To evaporate the acetone out of the solution, the bottle with the sample was placed in a ventilated oven at 60°C overnight. This mixture was always kept in the dark to avoid the bleaching of the fluorescent dye.

Structures are printed using Photonic Professional GT2, Nanoscribe GmbH onto 22 mm × 22 mm ITO coated, 170 μm thick glass (Diamond Coatings), using a 63× objective (Zeiss - 1.4 NA Oil Dic, Plan polycromat). The substrates are placed into the machine sample holder, and a small amount of photo-resin IPS (Nanoscribe GmbH) is drop casted onto the substrates. The sample holder is then loaded into the machine with the resin side facing the objective. Next, the objective is moved toward the substrate, and the interface is found automatically. The designed tapered waveguides were printed using dip-in laser lithography (DiLL) mode. In this mode of printing, the IR printing beam always passes through the non-polymerized resin. To ensure optical quality of the prints, the hatching and the slicing values were set to 100 nm to ensure maximum overlap of the voxels. After a layer was printed, contouring was performed along the edges of each slice. After the printing is completed, the substrates were developed in propylene glycol methyl ether acetate (PGMEA) solvent (Sigma Aldrich) for 20 min to remove the unpolymerized resin, followed by 5 min in isopropanol, and the structures were then dried at room temperature.

The waveguides were imaged using scanning electron microscopy (SEM). The substrates with the DLW printed waveguides were cut to the appropriate size and coated with the 8 nm of Au/Pd mixture. The imaging was performed using Thermo Fisher Verios 4G HP Schottky field-emission SEM with monochromator, utilizing secondary electrons (SEs) to reveal the morphology and topography of the imaged structures. The printed structures were imaged either from the top or tilted by 30 deg to obtain the side view.

The printed polymer structures were coated with CYTOP (CTX-809AP2, Asahi Glass Co., Ltd.), with a refractive index of 1.34. The printed structures were dipped into a 0.6% (mass fraction) solution of CYTOP in solvent CT-Solv. 180 (Asahi Glass Co., Ltd.). After dipping, the substrates were heated at 110°C for 2 h. This produces a $\sim$5 nm thick fluoropolymer film on the surface of the structures.

A mixture of water and glycerol in a weight ratio of 1:0.08, along with 8.2 mmol/L SDS, was prepared to match the density and prevent the LC droplet from floating away. The substrates containing the CYTOP-coated polymer scaffolds were placed on the microscope stage (Nikon Eclipse, Ti-U). A large droplet ($\sim$100 μL) of the water-glycerol mixture with SDS was then injected onto the printed area using a micropipette. The dye-doped LC mixture (2 to 3 μL) was loaded into the micro-injection tip, which was submerged in the water-glycerol solution, as shown in Fig. S3 in the Supplementary Material. The injection pressure (p_i), injection time (t_i), and compensation pressure (p_c) were adjusted to 3000 hPa, 0.6 to 1.0 s, and 30 hPa, respectively.

The optical setups used for this experiment are shown in Figs. 2 and 3. Figure 2 presents the beams that illuminate

Table 1 Details of the liquid crystals used in the experiments.

Liquid crystal	Producer	Extra-ordinary refractive index (n_e)	Ordinary refractive index (n_o)	Birefringence (Δn)	Nematic to isotropic temperature (T_{NI})
MLC-2132	Licristal, Merck KGaA, Darmstadt, Germany	1.77	1.51	0.26	114°C
E7	SYNTHON Chemicals, Germany	1.7378	1.5183	0.2195	61°C
5CB (4-cyano-4’-pentylbiphenyl)	Yantai Xianhua CHEM-TECH. Co., Ltd., China	1.71	1.54	0.17	35°C
XV9012-A00	Qingdao GRANDINCHEM Corp., China	1.549	1.479	0.07	84°C
HNG7172-00-000	HCCH, Jiangsu Hecheng Display Technology Co., Ltd., China	1.513	1.474	0.039	82°C

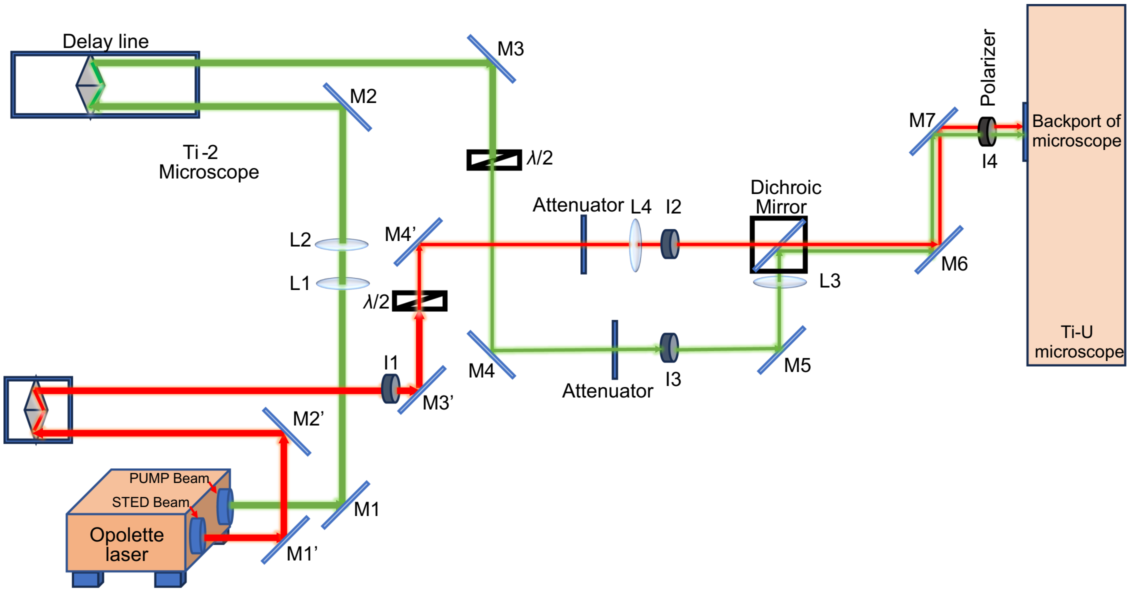

Fig. 2 Optical setup showing the path of the Excitation (PUMP) beam and STED beam from the Opolette Laser unit entering the microscope through the port at the back side of the microscope, allowing their alignment on the sample plane.

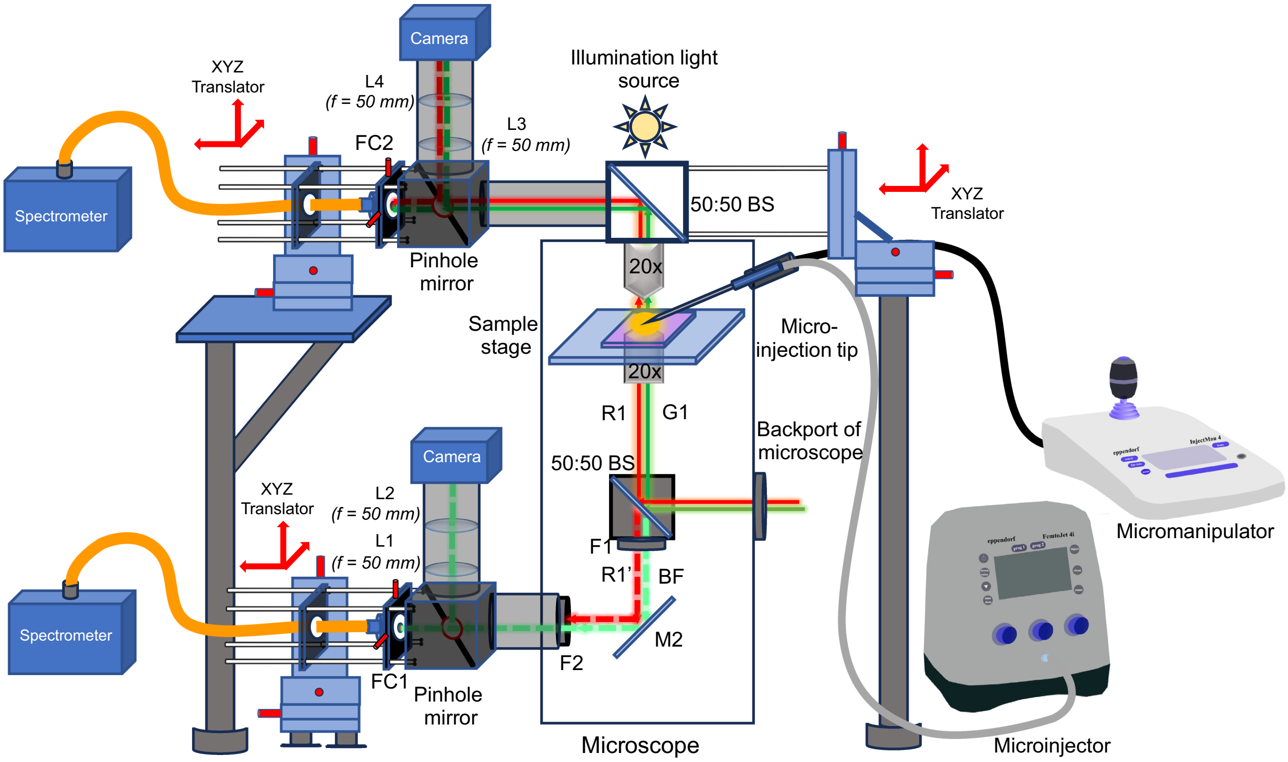

Fig. 3 Complete setup with attached assemblies at the top side above the sample plane and bottom side with the left port of the microscope to capture the image and collect the spectra in the reflection and transmission sides. The microinjection setup is also attached to the microscope.

the sample, whereas Fig. 3 shows two separate detection systems that collect the light in transmission and reflection, respectively. Figure 2 shows the path of the excitation (PUMP) beam and tunable STED beam from the two separate exits of the Opolette Laser box to the entrance of the inverted microscope (Nikon Eclipse, Ti-U) at the back port. In the schematic, M1 to M7 and M1' to M4' are the mirrors used in the path of the PUMP beam and STED beam, respectively, to direct the beam path. The PUMP beam is sent through a delay line to allow for setting a variable time delay between the PUMP and STED pulses. The delay line is made of a retroreflector mounted on a linear translation stage. I1 to I4 are the iris diaphragms used in the setup to adjust the light stops for alignment and filtering purposes. The L1, L2, L3, and L4 are the lenses with focal lengths 100, −75, 400, and 400 mm, respectively. One dichroic mirror is used where both PUMP and STED beams are joined to reflect the 532 nm wavelength and transmit the above wavelengths.

Further, these beams are aligned properly through the back port of the microscope to the sample plane by sending them through the 50:50 beamsplitter (BS) fixed into the microscope and focused to the sample plane using a 20× objective (Plan, Fluor, Nikon), as shown in Fig. 3. Along with this BS in the backward direction, one filter (F1) that cuts to the 532 nm wavelength is attached. At the exit of the left port of the microscope toward the bottom, one more filter (F2) is inserted to cut the wavelengths above 600 nm.

In Fig. 3, two detection assemblies are shown, which collect the light from the sample either in transmission or reflection. The light, reflected from the sample, or emitted in the backwards direction, is detected by a system attached to the bottom-left port of the microscope. A homemade pinhole Cr mirror (pinhole real size: 200 μm) is attached at 45 deg to reflect light from the objective toward the camera. The pinhole was designed of elliptical shape to appear circular when viewed with the camera. The camera (Flir, BS Blackfly BFS-U3-80S5C, Richmond, BC, Canada) is attached above the pinhole mirror aligned at a 45 deg angle, and in between the pinhole mirror and camera there is a pair of lenses (L1, L2) with focal lengths of 50 mm to focus the image on the camera appropriately. On the camera image of the sample, we can clearly see the pinhole as a dark circle. This makes it possible to align the pinhole with the region of interest (ROI) on the sample with great precision. Any light from the ROI that falls onto the pinhole is transmitted to the pinhole and collected with a multimode waveguide that was connected to the entrance slit of a spectrophotometer (Andor Shamrock SR-500i, Belfast, Northern Ireland) equipped with a cooled EM-CCD camera (Newton DU970N, Andor, Belfast, Northern Ireland). The optical coupler of the optical waveguide was mounted on a precision xyz translator, which was used for fine alignment of the optical axis of the light collecting coupler and the pinhole. This was made by searching for the maximum of detected intensity of light. The light, transmitted through the sample, or emitted in the forward direction, is collected by a separate optical system, designed on several solid optical mounts with a platform above the microscope. A very solid mechanical support was designed, to reduce mechanical vibrations, which are present even on the optical table, where the whole setup is mounted. The light collecting assembly on top is similar to the light collecting assembly on the bottom-left port of the microscope, as shown in Fig. 3.

Along with these light-collecting assemblies, the microinjector and micromanipulator are attached to the microscope with a microinjection tip to inject the microdroplets between the printed waveguide scaffolds. As mentioned earlier, a microinjector (FemtoJet 4i, Eppendorf) is used to control the size of the droplet by adjusting the injection pressure (p_i), injection time (t_i) and compensation pressure (p_c) values. Micromanipulator (InjectMan 4, Eppendorf) controls the position of the microinjection tip with a motor step size of <20 nm.

To measure the lasing threshold of the whispering gallery mode (WGM), the pump beam (532 nm) from the Opolette X tunable laser system (Opotek) was used; see Fig. 2. The energy of the pump beam was computer-controlled and measured with an energy meter (Ophir PD10-C, range 1 nJ to 1 μJ and Ophir PD10-pJ-C, range 10 pJ to 200 nJ). The pump beam was directed through the waveguide to excite the dye molecules and generate fluorescence within the sphere. An abrupt increase in output was noted after reaching the knee point on the intensity versus pump energy graph. Each data point represents the average of 100 sets of measurements, and error bars represent the standard deviation from the mean of the plotted quantity.

The WGM lasing depletion was observed using the STED wavelength of 605 nm. The pulse energy of the STED beam was computer controlled and measured with an energy meter. The dye-doped liquid-crystal droplet, positioned between the waveguide scaffolds, was illuminated with ∼1 to 2 nJ pulses above the lasing threshold through one of the waveguides. The WGMs were imaged using a camera, and spectra were collected through a diagonally opposite waveguide, as shown in Fig. 3. The time delay between the STED and PUMP pulses was adjusted to zero, with a precision of ∼100 ps.

3 Results

We use direct laser writing (DLW)[23–28] to print a group of four tapered polymer optical waveguides, standing upright on a glass substrate, as shown in Figs. 4(a) and 4(b) (see also Video S2). The cylindrical tapered waveguides are 45 μm high, with a base diameter of 8 μm, cone angle of 5.5 deg, and waveguide diameter of 2 μm. Printing details are available in the Supplementary Material, Figs. S1 and S2. The refractive index of the waveguides is 1.5, which gives the angle of acceptance of ∼44 deg in air. The waveguides are coated by a 5-nm layer of fluorinated polymer (CYTOP, see Sec. 2). The CYTOP-coated waveguide scaffolds are submersed in a solution of water and glycerol. The mass ratio of water and glycerol is 25:2 to match the densities and prevent buoyancy-driven lift-off of LC droplets during the experiments. We used five different LCs, as listed in Table 1. Each LC has been doped with a small concentration of fluorescent molecules that align with their radiative dipole moment parallel to the LC molecules, and the SDS surfactant in the water/glycerol mixture induces perpendicular orientation of liquid-crystal molecules at the surface of the droplet. A dyed LC droplet is inflated inside the 4-waveguide (see Sec. 2 and Video S1), softly touching the four tapered waveguides [Fig. 4(c)], which provides efficient coupling of light between the waveguides and the droplet [Fig. 4(d)]. The CYTOP coating prevents the wetting of polymer waveguides with the dyed LC droplet, providing robustness and structural stability over the many days of experiments (Video S3).

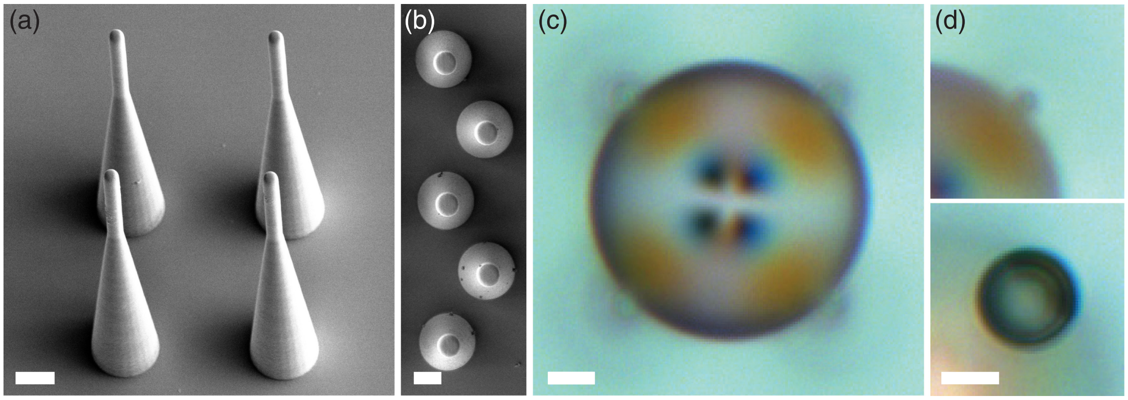

Fig. 4 WGM cavity light switch. (a) SEM image of a DLW printed scaffold of four tapered polymer waveguides, side view with the sample tilted 30° (see Sec. 2 for details). (b) Top view of another set of printed polymer waveguides. (c) A scaffold of tapered polymer waveguides hosting dyed LC droplet. (d) Zoom-in microscope view, focused on top (upper panel) and base (lower panel) of the tapered waveguide in the upper-right corner of (c). Scale bars in (a)–(d) represent 5 μm.

A pulsed Nd:YAG laser (Opolette HE 355 LD, Opotek), with an optical parametric oscillator (OPO) was used to generate both frequency-doubled (532 nm) and tunable pulsed beams (410–2400 nm). A complex optical setup provided intensity and polarization control and accurate setting of the time delay between the excitation (532 nm) pulses and STED pulses from the OPO; for details, see the Supplementary Material. The sample was placed on a microscope stage (Eclipse Ti-2E, Nikon, Tokyo, Japan), and a 20× objective (Nikon Plan Fluor, Tokyo, Japan) was used to focus both beams on the tapered waveguides. The average spot sizes were ~6.9 μm for the 532-nm beam and ~14.2 μm for the tunable beam from the OPO.

The coupling of light from tapered waveguide into the dyed LC droplet is a critical aspect of this work. If the waveguide and the cavity were made of solid materials, the contact area between a sphere (diameter ~28 μm) and the cylindrical waveguide (diameter ~2 μm) would be vanishingly small. This means that the electromagnetic fields in the cavity and waveguide could be coupled only via evanescent light fields, which emanate to ~100 nm from each surface. However, in our case the spherical cavity is made of an LC that does not preserve spherical shape, when it comes in contact with the cylindrical waveguide. Because of the liquid nature of the LC droplet, the interfacial forces and the corresponding contact angle determine the actual 3D shape of the waveguide-LC droplet contact. Although the liquid crystal orientation might be elastically distorted in this near-contact area, the corresponding elastic energy of distortion is expected to be several orders of magnitude smaller compared to surface energies and can be ignored. In our optical study of fiber-droplet contact, we observed very similar behavior of isotropic droplets (made of immersion oil) and liquid crystal droplets in contact with cylindrical fiber. We could also see no elastic distortion of the liquid crystal in the vicinity of the contact with the fiber; see Figs. S4 and S5 in the Supplementary Material, and Video S9 in Appendix B. We should note that the shape of the contact line and the corresponding interfacial surfaces are nontrivial in 3D, since the cylindrical polymer waveguide is in contact with a liquid sphere.

The transfer of the excitation light and the onset of WGM lasing are presented in Fig. 5 (Video S4). When the surface of the droplet is far away from the waveguide [~10 μm, Fig. 5(a)], no light is detected. Upon approaching, a very faint fluorescent light can be seen at a surface separation of less than one micrometer. However, by making a single step [3rd and 4th panel in Fig. 5(a)], the droplet approaches the waveguide for less than a micrometer, and the WGM lasing is clearly initiated during this single step. This suggests very tight confinement of the 532-nm excitation light to the waveguide and a very efficient coupling of pump light into the LC droplet.

The nature of the contact between the dyed LC droplet and the tapered waveguide is further revealed in Fig. 5(b) (Video S4), which shows a small area of the droplet boundary approaching the waveguide. When the droplet is at a separation of ~1 μm from the waveguide, the surface of the droplet appears to be attracted to the waveguide (see Video S5), and establishes a stable contact with the waveguide surface at a nearly normal contact angle $\theta \sim 90$ deg [Fig. 5(b)]. The last panel of Fig. 5(b) shows substantial overlap between the sphere (LC) and waveguide (polymer), providing an efficient flow of light from the waveguide to the cavity and vice versa.

Figures 5(c) and 5(d) show the images and corresponding spectra while the droplet approaches the waveguide. Light is collected through the pinhole, large dark spot in the images. We can clearly see the onset of WGM lasing both in images [Fig. 5(c)] and captured spectra of light [Fig. 5(d)]. There is an interesting detail in images of lasing: the emitted light appears grainy, as compared with smooth appearance of pure fluorescence at low pumping fluences. This grainy structure of emitted light is a typical indication of the spatial coherence of light and thereby an indirect indication of lasing. Overall, Fig. 5 demonstrates a very efficient coupling of light between a cylindrical tapered waveguide and a spherical LC cavity, which is reflected in very low WGM lasing threshold fluences, as follows.

Figure 6 shows visual evidence for the onset of WGM lasing from a droplet of pyromethene 580 (PM 580)-doped E7 LC, confined within the four tapered waveguides, touching the surface of the droplet, as shown in Fig. 6(a); see also Videos S6 and S7. As shown in Fig. 6(b), the pump pulses were sent through the base of the upper-right waveguide in Fig. 6(a) with increasing pump fluence. At low fluence [the first panel in Fig. 6(b)], we can observe smooth and faint fluorescence caused by the

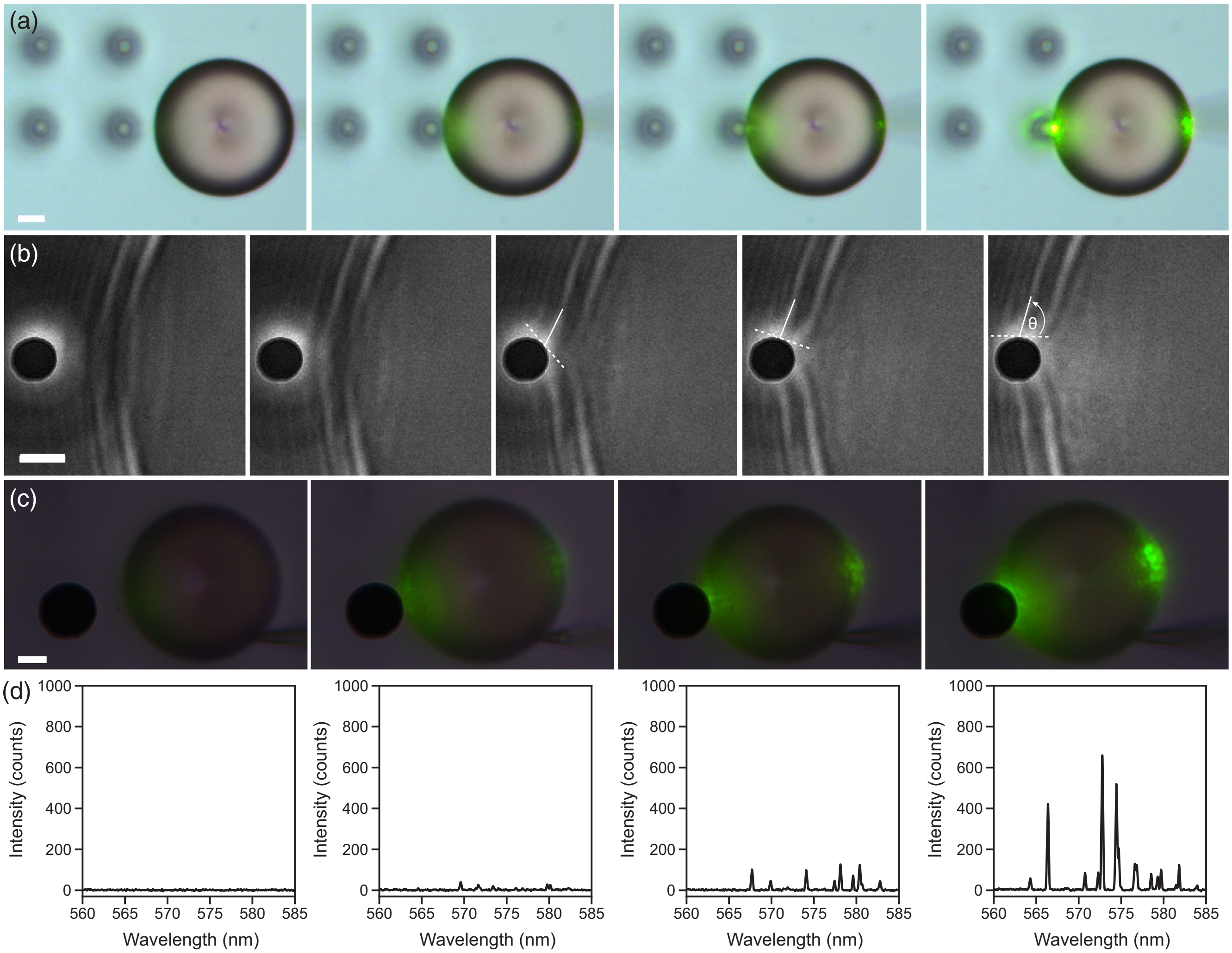

Fig. 5 Coupling light into WGM cavity light switch. (a) Images under bright illumination showing the coupling of light from the tapered waveguide to the LC droplet fixed to a micropipette as the droplet approaches the waveguide and initiates WGM lasing at a sufficiently small surface separation. Scale bar is 10 μm. (b) Close up image of the droplet boundary making contact with the waveguide indicating close to normal contact angle between the two surfaces (Video S5). Contact angle θ between the LC droplet and fluorinated waveguide is estimated to $\sim$90 deg. This apparent contact angle could be influenced by optical aberrations of light on polymer waveguide and liquid crystal droplet. Scale bar corresponds to 2 μm. (c) Images under low back-illumination of a droplet approaching the tapered waveguide. The dark circle is the pinhole that collects light from the waveguide. Note the characteristic speckles indicating coherence of the emitted green light. Scale bar is 10 μm. (d) Spectral analysis corresponding to (c), with spectra illustrating the uncoupled state when the LC droplet and the waveguide are far apart, and the emergence of WGMs as the droplet approaches the excitation beam sent through waveguide, indicating increased light coupling efficiency. Note: the 532-nm pump light is blocked on all images by using an optical density (OD) 6 notch filter centred at 532 nm.

532-nm light. By increasing the pump fluence, we can clearly see not only increased overall fluorescence intensity but also characteristic speckles in the emitted light. The presence of speckles indicates coherence of light emanating from the droplet, which is a clear signature of WGM lasing at sufficiently strong pump fluence.

WGM lasing threshold is characterized by measuring spectra when increasing the fluence of the pump beam. The light emitted from the same waveguide that is used for excitation is captured through a small pinhole, focused into a multimode fiber, and sent to the entrance slit of a spectrophotometer. Figure 7(a) shows a 2D color map of WGM spectra of E7 nematic droplet as a function of 532-nm pump fluence. The corresponding integral of WGM lines intensities is presented in Fig. 7(b) as a function of pumping fluence. We can clearly see the onset of WGM lasing [see also zoom-in in the inset

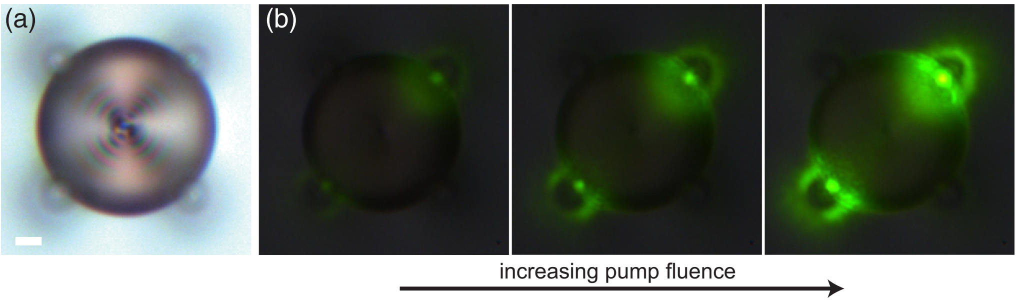

Fig. 6 Lasing from WGM cavity light switch. (a) A droplet of E7 nematic LC is confined to a scaffold of four tapered polymer waveguides under parallel polarizers. Scale bar 1 μm. (b) Visual observation of the onset of WGM lasing in dyed E7 droplets confined to a scaffold of four tapered polymer waveguides by increasing the 532-nm pump fluence. The 532-nm light is blocked using a high OD notch filter.

to Fig. 7(b)] at fluence of less than 10 pJ/μm^2. The lowest lasing threshold in E7 droplet is found for the WGM mode at 579.2 nm, which is shown in Fig. 7(d). The threshold for lasing of this particular mode is at only $\sim$3 pJ/μm^2 fluence, which is an extraordinarily low lasing threshold. For example, CLC dye lasers typically have lasing thresholds[29] of the order of $\sim$100 pJ/μm^2. The very low WGM lasing thresholds in nematic droplets coupled to tapered polymer waveguides indicate very efficient excitation of dyed LC in the cavity-waveguide system. For comparison, we have also measured WGM lasing threshold for direct excitation, i.e., by directly focusing the 532 nm beam onto a dyed LC 5CB with 0.2% (mass fraction) PM580 dye droplet. The corresponding WGM lasing thresholds were $\sim$21 pJ/μm^2, whereas lasing via waveguide excitation is observed already at a lower fluence of $\sim$11 pJ/μm^2. It is difficult to observe the transition from the amplified spontaneous emission (ASE) to lasing, because for a single pulse the count rate of ASE fluorescence is exceedingly small. However, a direct indication of lasing regime is the narrowness of WGM lines, which is typically less than 0.22 nm, and clear presence of the lasing threshold. It is interesting that above the lasing threshold, the lasing lines shift towards the blue side of the spectrum with increasing pumping fluence, which we attribute to the optical Kerr effect in an LC, i.e., linear change of the refractive index in intense electric field of the light pulse.[30]

The STED principle is best known from STED super-resolution microscopy[15] and is based on the precise timing of two consecutive light pulses that control the fluorescence emission from the fluorescently labeled sample. STED principle was recently used to control laser emission from CLC micro-lasers using nanosecond light pulses.[16] We have already shown in Fig. 1 details of WGM lasing emission control from the dyed LC droplets containing photo-excited fluorescent molecules. Briefly, after a 532-nm nanosecond pulse excites the fluorescent molecules in Fig. 1(a), WGM lasing is initiated within the droplet. The WGM resonant waves can be considered as light circulating clockwise and anti-clockwise via total internal reflection at the droplet-water interface. Because of the coupling of tapered waveguides with the droplet, WGM light will leak out through the waveguides. However, if another, nanosecond pulse that has the wavelength red-shifted compared with fluorescence emission peak (i.e., stimulated emission depletion or STED pulse), is sent through the same tapered waveguide to circulate inside the droplet before WGM laser emission takes place [Fig. 1(b)], this STED light will induce electronic transitions from the excited to the ground electronic states of the fluorescent molecules through the process of stimulated emission, and will empty the excited electronic states. This means there will be no energy available for lasing emission, and no light will be emitted through the WGMs. All of the energy that was available for WGM lasing is now used to amplify the STED pulse at λ_{STED}.

The results of STED experiments in dyed E7 droplets are shown in Fig. 8. Figure 8(a) presents a WGM spectra integral intensity map taken at the $\sim$8.4 pJ/μm^2 excitation fluence of a single 532-nm pulse, in dependence on the fluence of STED pulse at $\lambda_{\mathrm{STED}} = 605$ nm. We can clearly see that the intensity of most WGM modes decreases as a function of increasing STED pulse fluence. This is more clearly seen in Fig. 8(b), which presents the integrated intensity of all WGM modes in Fig. 8(a) as a function of STED pulse fluence. At a STED fluence of $\sim$100 pJ/μm^2 the WGM lasing from all modes is nearly entirely depleted, with some of the WGM modes persisting. To get better insight into individual WGM mode depletion, we present in Fig. 8(c) the WGM spectra at different STED pulse fluence. Here, we select the mode at 582.1 nm and follow its intensity as a function of increasing STED pulse fluence, shown in Fig. 8(d). We can clearly see the nearly complete darkening of the 582.1-nm WGM mode at STED pulse fluence of $\sim$75 pJ/μm^2.

The experimental results presented in Fig. 8 clearly demonstrate the control of WGM lasing by using the STED concept in the dyed LC micro-droplet. The fluences needed to completely deplete the WGM lasing are of the order of $\sim$50 to 100 pJ/μm^2, which is an order of magnitude higher compared with the fluences needed to excite the WGM lasing. We measured STED attenuation of WGMs in a number of experiments on different droplets of different LC and dye concentration. The results are summarized in Table 2. It is indicative that the two low birefringence LCs XV9012-A00 ($\Delta n = 0.07$) and HNG7172-00-000 ($\Delta n = 0.039$) show significantly higher STED energies required for 50% WGM attenuation.

Although the spectra in Fig. 8 are measured by collecting and averaging over 100 repetitions, we present in Fig. 9 the depletion of WGM lasing by a single STED pulse. The depletion is exceptionally strong even on a single pulse scale, i.e., nanosecond scale, which promises efficient implementation of this depletion mechanism in more complex geometries involving several WGM micro-lasers, which are mutually interconnected.

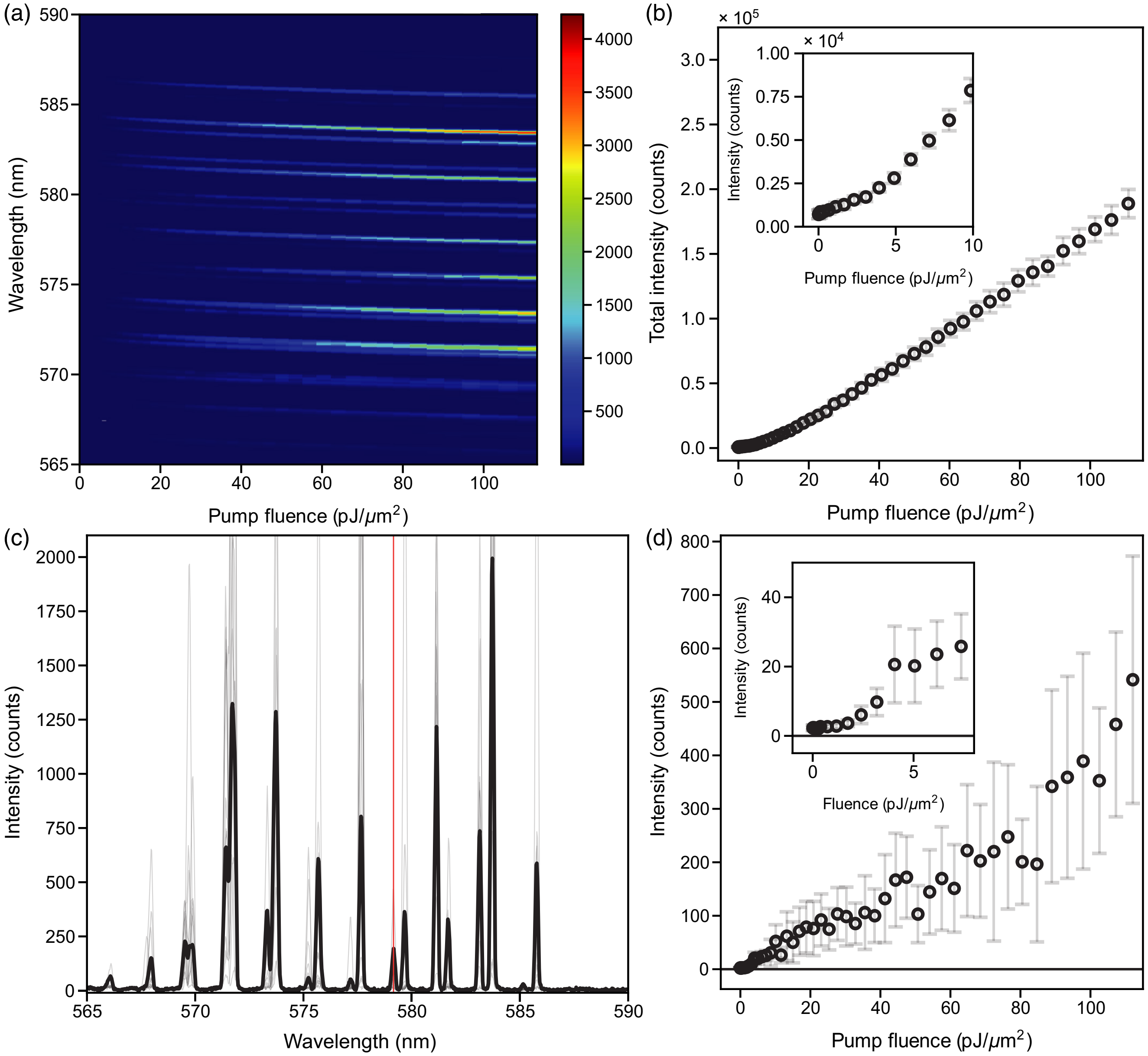

Fig. 7 Lasing threshold of WGM cavity light switch. (a) Map of the WGM lasing thresholds in a ~28 μm diameter microcavity made from dye-doped E7 nematic LC. Note the blue-shift of WGM resonances with increasing excitation fluence. The colour scale indicates the intensity counts of the detected light. (b) Measurement of WGM lasing threshold in ~28 μm droplets of dye doped E7 LC, inset shows the zoom-in view of lasing threshold region. The integral of all light intensity across the spectrum is plotted. (c) WGM spectrum at higher fluence (~60 pJ/μm^2) of excitation wavelength showing discrete wavelengths. The thick black spectrum represents the average of single-shot spectra for 100 pump pulses, with a few single-pulse WGM spectra shown as thin black lines in the background. Red vertical line corresponds to the peak at 579.2 nm. (d) Intensity of the lasing peak at 579.2 nm as a function of the pump fluence. This is the lowest lasing threshold WGM modes.

The experiments are further supported by numerical simulations. We model light propagation using the finite-difference time-domain (FDTD) method,[31] coupled with equations describing the interaction of light with the organic dye, as well as the spatial and temporal distribution of the occupancy of the dye's four energy levels; see Appendix A. The Meep software package[32] is employed. Due to the computational complexity, the simulations are performed in a simplified, two-dimensional cross-section of the nematic LC droplet between the two tapered waveguides, rather than in the full three-dimensional geometry. This approach still preserves the crucial properties of the resonator needed to prove the main ideas of this study. The diameter

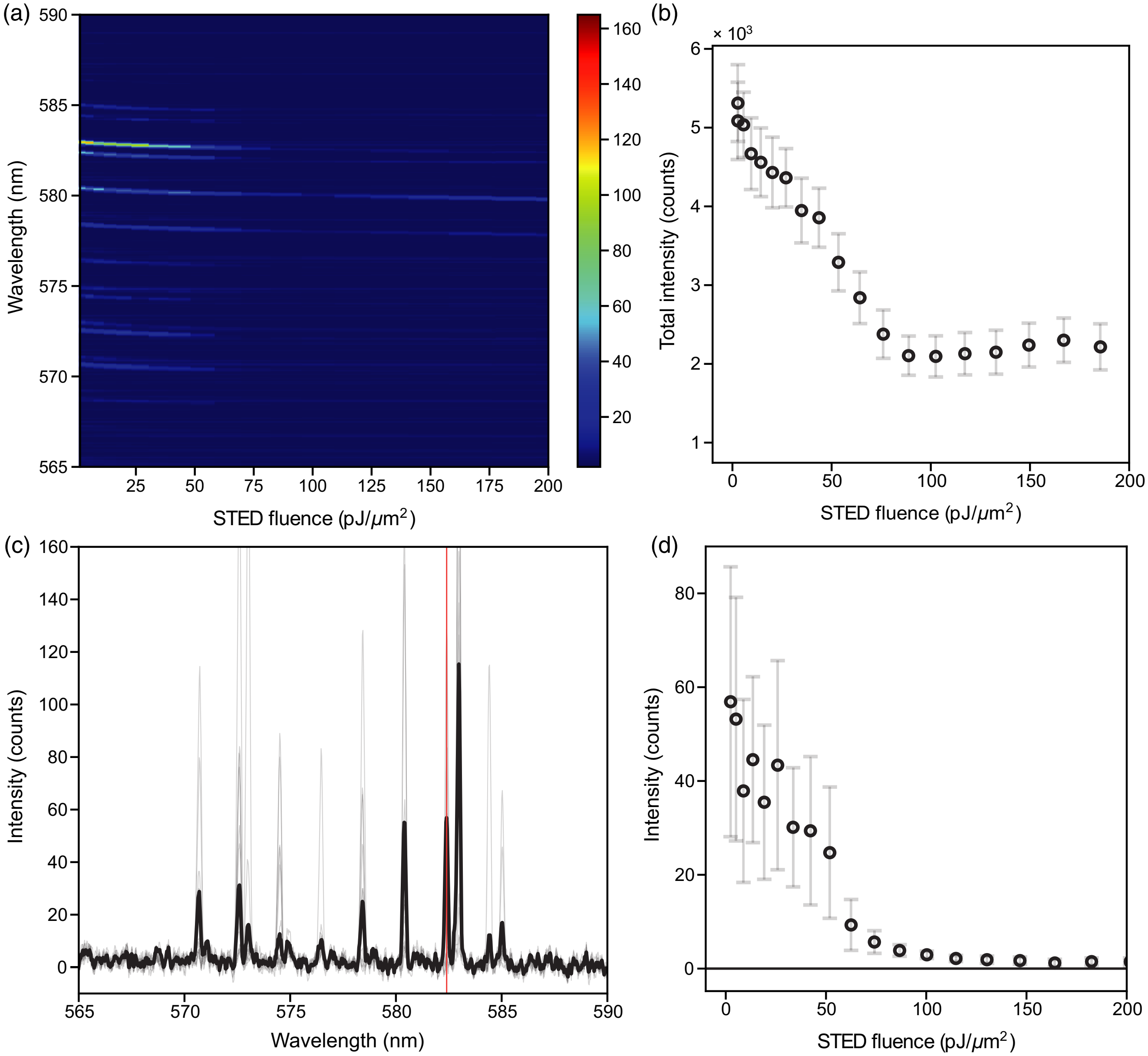

Fig. 8 Depletion of lasing from WGM cavity light switch. (a) Fluence of STED beam-induced depletion of the WGMs at discrete wavelengths and shift of WGM resonances in a ~28 μm diameter micro-resonator made from dye-doped E7 nematic LC. The colour scale indicates the intensity counts of the detected light. (b) Measurement of STED fluence required to deplete the WGMs obtained from ~28 μm droplets of E7 LC. (c) Intensity spectra of WGMs at ~2.8 pJ/μm^2 STED pulse fluence showing discrete wavelengths. The thick black spectrum represents the average of single-shot spectra for 100 pump pulses, with a few single-pulse WGM spectra shown as thin black lines in the background. Red vertical line corresponds to the 582.1 nm wavelength. (d) Reduction of the intensity of 582.1-nm WGM with the increase of STED pulse fluence.

of the nematic droplet with radial structure is 14 μm, and the refractive indices of the LC are $n_o = 1.474$ and $n_e = 1.513$. The absorption spectrum of the dye, which is dispersed in the LC is centred at 530 nm, whereas its emission spectrum peaks at 570 nm. All other relevant material parameters, the exact geometry, and the theoretical model of the saturable multilevel susceptibility of the dye are described in Fig. S7 in the Supplementary Material and in Appendix A.

Figure 10 shows light propagation in two operating regimes: in lasing [Figs. 10(a)–10(d) and in STED [Figs. 10(f)–10(i)]; see also Video S8. In both regimes [Figs. 10(a) and 10(f)], a pump pulse with a wavelength of 532 nm (shown in turquoise) and linear polarization along the x-axis is sent upwards along the y-axis through the right tapered waveguide. A fraction of this light couples into the droplet at the waveguide-droplet interface. The pump light trapped in the droplet travels in a counter-

Table 2 Measurements of lasing thresholds and STED fluences for 50% WGM peak attenuation, for several different droplets of different LCs and different dye concentrations.

Liquid crystal + Dye (%, mass fraction)	Droplet diameter (μm)	Lasing threshold fluence (pJ/μm^2)	Peaks observed during the STED experiment	PUMP and STED fluences	
				PUMP fluence (pJ/μm^2)	STED (605 nm) fluence (pJ/μm^2)
E7 + PM580 (0.2%)	~28	~8.4	Peak 1 (570.4 nm)	~8.4	~43.7
	~28	~8.4	Peak 2 (572.3 nm)	~8.4	~43.7
					~53.5
	~28	~8.4	Peak 3 (578.1 nm)	~8.4	~64.3
	~28	~8.4	Peak 4 (580.0 nm)	~8.4	~64.3
	~28	~8.4	Peak 5 (582.1 nm)	~8.4	~43.7
	~28	~8.4	Peak 6 (582.6 nm)	~8.4	~43.7
E7 + PM580 (0.0125%)	~28	~8.4	Peak 1 (564.9 nm)	~20.3	~64.3
E7 + PM580 (0.1%)	~28	~12.9	Peak 1 (570.3 nm)	~15.8	~88.8
	~28	~12.9	Peak 2 (572.4 nm)	~15.8	~76.1
HNG 7172-00-000 + PM580 (0.2%)	~28	~8.4	Peak 1 (577.2 nm)	~8.4	~167.1
	~28	~8.4	Peak 2 (579.2 nm)	~8.4	~292.1
XV9012-A00 + PM580 (0.2%)	~28	~9.8	Peak 1 (577.7 nm)	~20.3	~149.5
	~28	~9.8	Peak 2 (580.2 nm)	~20.3	~225.4
MLC-2132 + PM580 (0.2%)	~28	~14.7	Peak 1 (568.2 nm)	~44.3	~76.1
	~28	~14.7	Peak 2 (575.7 nm)	~44.3	~117.2
					~132.9
5CB + PM580 (0.2%)	~28	~11.3	Peak 1 (573.5 nm)	~11.3	~14.3
					~20.2
	~28	~11.3	Peak 2 (574.0 nm)	~11.3	~14.3
					~20.2
	~28	~11.3	Peak 3 (577.1 nm)	~11.3	~14.3
					~20.2

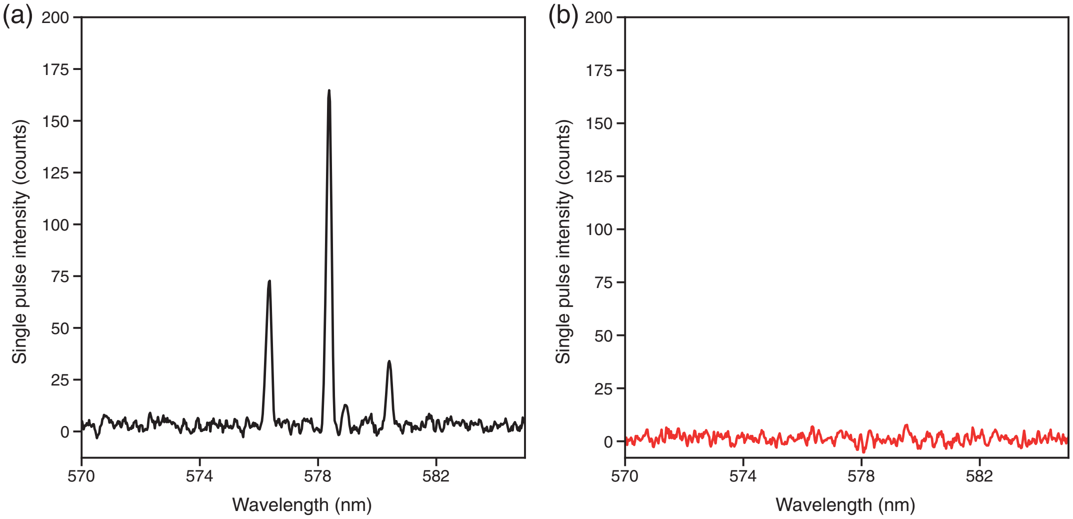

Fig. 9 Single light pulse depletion in WGM cavity light switch. (a) Single pulse WGM lasing is initiated by a 532-nm pump pulse of ~27 pJ/μm^2 fluence, i.e. slightly above the lasing threshold for the droplet of 0.2% (mass fraction) PM580 dye-doped E7 LC. (b) Single STED pulse depletion of WGM lasing. The fluence of STED pulse is ~890 pJ/μm^2.

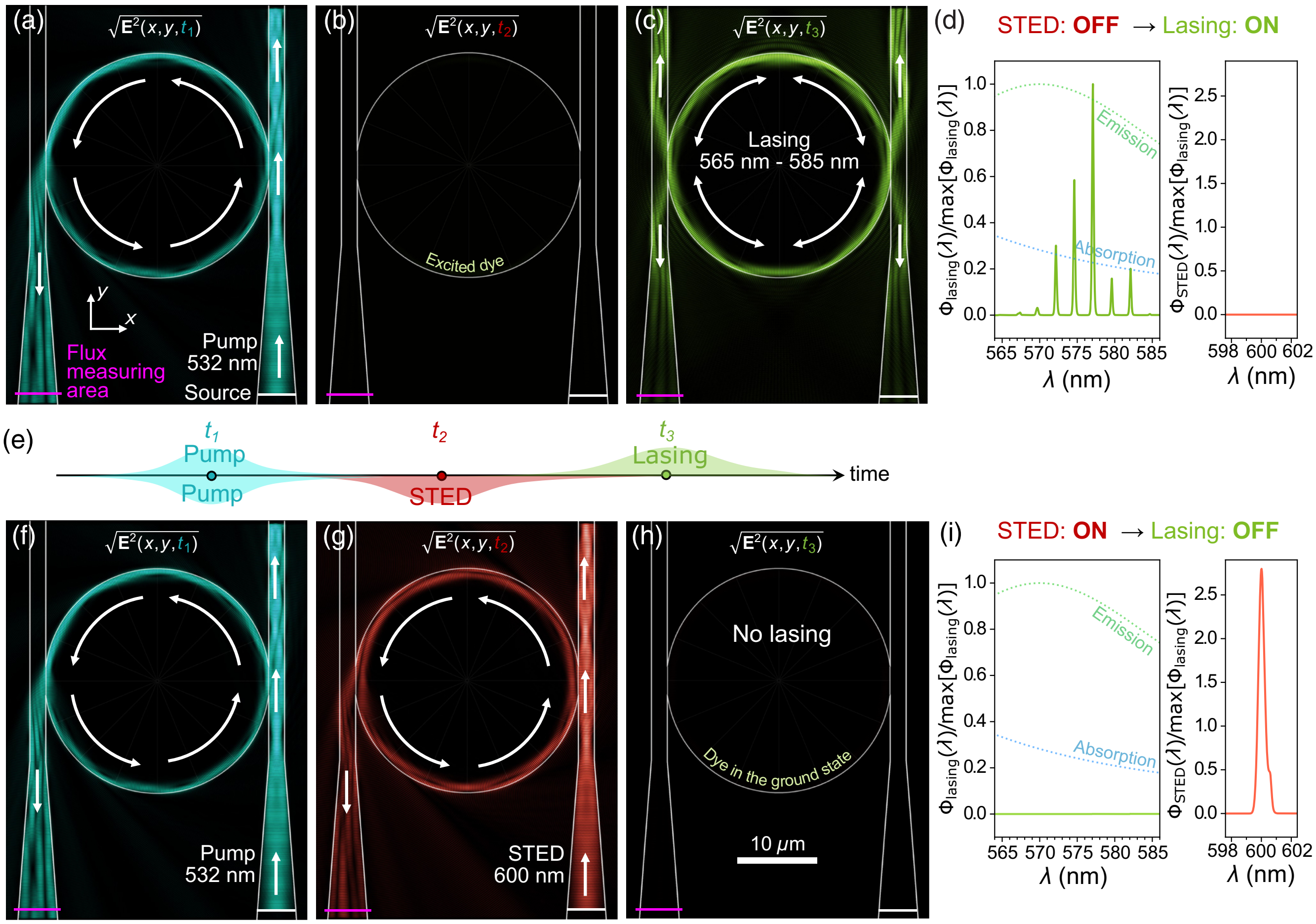

Fig. 10 Numerical simulation of WGM lasing and STED. (a)–(c) The electric field $\sqrt{E^2(x,y)}$ in lasing regime at selected times. Pump pulse (532 nm) is shown in turquoise, while laser light (565–585 nm) in green. (d) Cumulative spectrum of light propagated through the flux measuring area at the bottom of the left waveguide in lasing regime. If STED is turned off, spectrum at 600 nm is zero (in orange) and characteristic WGMs appear in the 565–585 nm range (in green). The green dotted line in the background represents the dye's emission spectrum, while the blue dotted line corresponds to its absorption spectrum. (e) Schematic of the time sequence of pump, STED, and lasing. (f)–(h) Time sequence of electric field $\sqrt{E^2(x,y)}$ in STED regime with STED light (600 nm) shown in orange. (i) Cumulative spectrum of light in the presence of STED with suppressed lasing in 565–585 nm range (in green) and non-zero spectrum around 600 nm.

clockwise direction around its perimeter. The light is partially absorbed, thereby exciting the dye molecules, while also leaking out downwards through the left waveguide and upwards through the right waveguide. The excited dye molecules around the droplet's perimeter enable the amplification of multiple WGMs within the dye's emission spectrum (around 570 nm), resulting in a WGM laser pulse. As long as enough excited molecules remain available, the laser pulse continues to amplify.

Figure 10(c) presents a snapshot of the multi-mode laser light (in green) at a selected time near its peak intensity. The generated laser light travels both clockwise and counterclockwise inside the droplet, leading to leakage into both waveguides in both upward and downward directions. The spectrum of the emitted laser light, measured at the bottom of the left waveguide (highlighted in magenta), is shown in Fig. 10(d). However, if the pump pulse is immediately followed by a STED pulse [Fig. 10(e)], sent through the same waveguide with the same polarization (x-direction) and at a wavelength of 600 nm, part of the STED light also couples into the droplet, where it induces stimulated emission [Fig. 10(g), in orange]. The STED pulse at 600 nm is thus amplified as it propagates counter-clockwise along the droplet's perimeter, while simultaneously driving the dye molecules back into the ground state. The STED pulse later weakens, as it runs out of excited molecules on which it can amplify, and due to the leakage from the droplet upwards into the waveguide on the right, and downwards into the waveguide on the left, as shown in Fig. 10(g). Because the STED pulse leaves the dye molecules in the ground state, lasing cannot evolve. This effect is evident in the spectrum [Fig. 10(i)] measured at the bottom of the left waveguide, where the WGM laser emission (565 to 585 nm) is completely suppressed by the STED pulse. Only the STED pulse at 600 nm and an additional WGM mode at ~600.6 nm, apparently induced by the STED pulse, remain visible in the spectrum.

The energy of the pump pulse E_{pump} sent into the waveguide is 2.152 times the threshold energy required for lasing $E_{\mathrm{thr.}}$ in both regimes shown in Fig. 10, and the energy of the STED pulse E_{STED} is 0.143 $E_{\mathrm{thr.}}$. The measured spectrum at the output waveguide can be controlled through these two parameters, as illustrated in Fig. 11. In the lasing regime, i.e., without STED, increasing the pump energy above $E_{\mathrm{thr.}}$ first leads to the appearance of four WGM modes in the spectrum, at wavelengths between 575 and 583 nm. With further increase in $E_{\mathrm{pump}}/E_{\mathrm{thr.}}$, additional modes in the range of 565 to 575 nm gradually amplify to lasing, as shown in Fig. 11(a). The total lasing energy, i.e., the integral of the spectrum, is presented in Fig. 11(c), which exhibits a characteristic laser threshold as well as the saturation of lasing energy. When the pump is sufficiently strong, it excites all available dye molecules along its path, therefore further increasing the pump energy does not lead to an increase in lasing energy. Figure 11(b) illustrates how WGM modes are suppressed when pumped at $E_{\mathrm{pump}}/E_{\mathrm{thr.}} = 2.152$ while gradually increasing the STED pulse energy E_{STED}. The first modes to disappear are those that were the last to emerge as E_{pump} was increased in the absence of STED. An energy of approximately $E_{\mathrm{STED}}/E_{\mathrm{thr.}} \approx 0.11$ is already sufficient to completely suppress all WGM modes. The total lasing energy as a function of increasing STED energy is shown in Fig. 11(d).

Finally, we numerically investigate the efficiency of coupling the light in and out of the droplet and the corresponding WGM lasing thresholds. The contact between the pillars and the nematic droplet strongly affects the lasing and STED performance of the studied optical micro-device. In the 2D simulations presented above, we use a geometry in which the pillar overlaps the droplet for 0.1 μm so that the droplet is slightly truncated, as shown in Fig. S7 in the Supplementary Material. To explore the influence of a changing contact geometry, we now vary the distance between the pillar and the droplet δ, as introduced in Fig. 12(a). In the results reported above in Figs. 10 and 11, in the reference geometry, this parameter is $\delta = -0.1$ μm.

Changing the parameter δ affects two quantities that are crucial for lasing and STED. First, it changes the amount of pump or STED light that is coupled at the contact from the waveguide into the droplet, where the light can interact with the dye. If, by tuning the distance δ, we increase the fraction of light coupled from the waveguide into the droplet, the laser can be switched on with a weaker pump pulse, i.e., the lasing threshold would be reduced. Second, δ also affects the Q-factors of the resonant WGMs that are excited in the droplet and emit the laser light. Moving the waveguides closer to the droplet makes it easier for light to leak out of the droplet, which lowers the Q-factors and typically increases the lasing threshold.

Figure 12(b) shows the ratio between the pulse energy E_1 measured at the end of the right waveguide when a droplet is positioned next to it at a distance δ and the pulse energy E_0 measured at the end of the same waveguide in the absence of the droplet, as illustrated in Fig. 12(a). Figure 12(c) shows the analogous ratio between the pulse energy E_2 measured at the

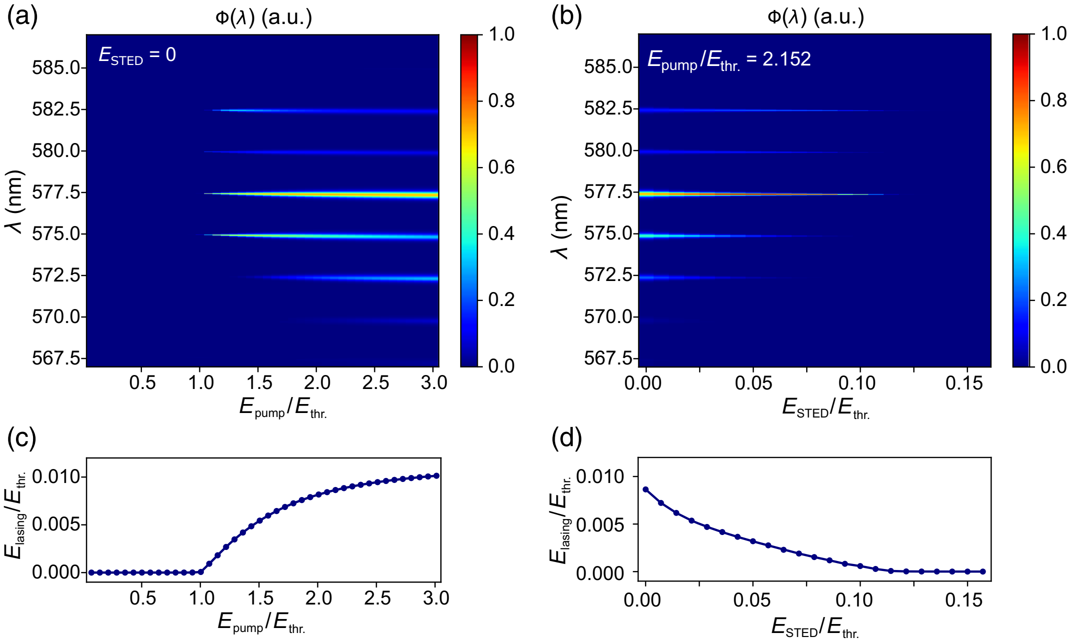

Fig. 11 Lasing and depletion of WGM spectral lines. (a) Lasing spectrum $\Phi(\lambda)$ in the absence of STED as a function of increasing pump energy E_{pump}, normalised to the threshold pump energy required for lasing $E_{\mathrm{thr.}}$. (b) Lasing spectrum $\Phi(\lambda)$ at fixed pump energy $E_{\mathrm{pump}}/E_{\mathrm{thr.}} = 2.152$ and increasing STED energy $E_{\mathrm{STED}}/E_{\mathrm{thr.}}$. (c) Total lasing energy $E_{\mathrm{lasing}}/E_{\mathrm{thr.}}$, the integral of the spectrum $\Phi(\lambda)$, in lasing regime for increasing $E_{\mathrm{pump}}/E_{\mathrm{thr.}}$. (d) Total lasing energy $E_{\mathrm{lasing}}/E_{\mathrm{thr.}}$ in STED regime for increasing $E_{\mathrm{STED}}/E_{\mathrm{thr.}}$ at a fixed value of the pump energy $E_{\mathrm{pump}}/E_{\mathrm{thr.}} = 2.152$.

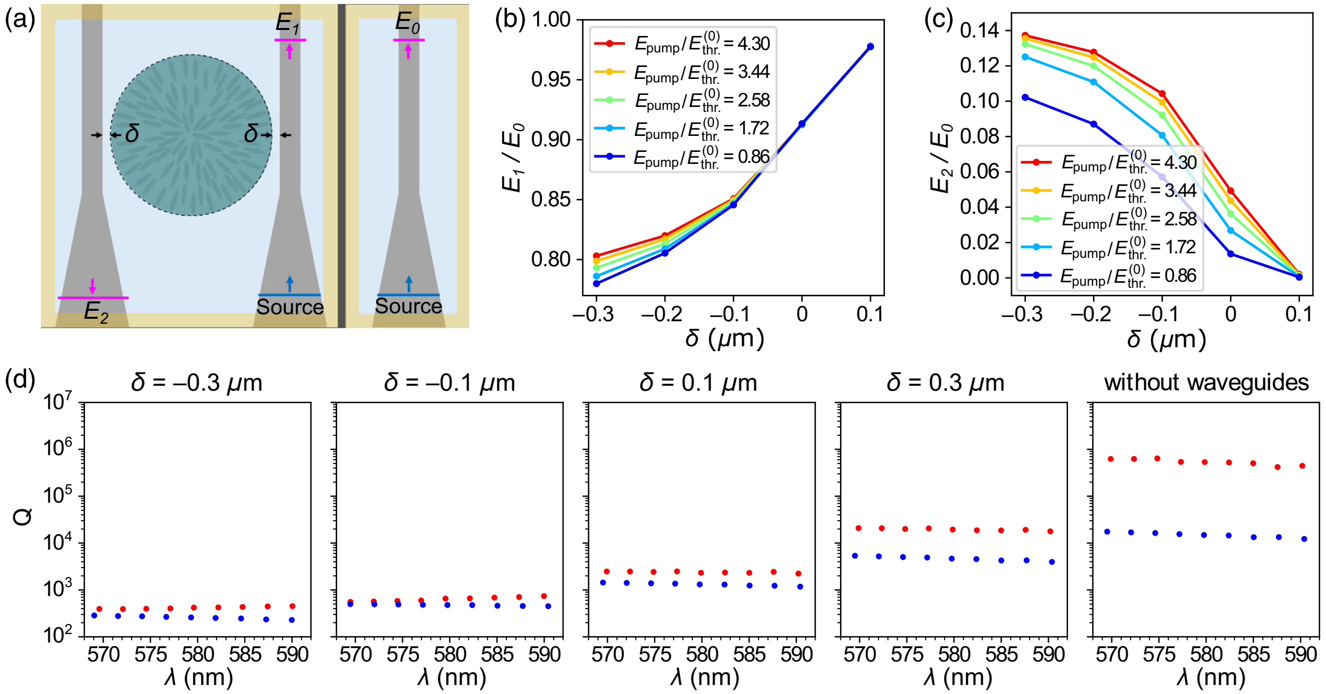

Fig. 12 Influence of droplet–waveguide separation on light coupling between waveguides and droplet and Q-factors. (a) Schematic of the 2D simulation geometry with the nematic droplet placed between two waveguides. The separation between the waveguides and the droplet surface is denoted by δ. (b) Ratio between the pump pulse energies measured at the end of the right waveguide with a droplet at a distance δ and at the end of the waveguide in the absence of a droplet, for several pump pulse energies normalized to the lasing threshold pump pulse energy in the reference geometry with $\delta = -0.1$ μm. (c) Ratio between the pump pulse energies measured at the bottom of the left waveguide and at the top of the right waveguide in the absence of the droplet. (d) Spectra $Q(\lambda)$ of the first-order whispering-gallery modes in the droplet for different waveguide-droplet separations δ and for the case without waveguides.

bottom of the left waveguide (for light propagating downwards) and the same reference energy without the droplet E_0. When the light is sent upwards through the right waveguide, part of it is scattered into the surroundings at the contact, whereas another part is coupled into the droplet, where it circulates along the inner side of the droplet's edge in the counter-clockwise direction and interacts with the dye. On the right-hand side, the light then leaves the droplet and propagates upwards through the right waveguide, whereas on the left-hand side it leaves the droplet into the left waveguide and propagates downwards.

As demonstrated in Fig. 12(b), the ratio E_1/E_0 increases when the droplet-waveguide distance δ is increased, whereas the ratio E_2/E_0 decreases, as shown in Fig. 12(c). The more strongly the waveguides are pressed into the droplet (negative δ), the larger the fraction of light that leaves the right waveguide and enters the droplet, and consequently, the more light reaches the bottom of the left waveguide. In Figs. 12(b) and 12(c), the energy ratios E_1/E_0 and E_2/E_0 are shown for several pump pulse energies E_{pump} sent upwards through the right waveguide, normalized to the threshold pump pulse energy $E^{(0)}_{\mathrm{thr.}}$ for lasing in the reference geometry with $\delta = -0.1$ μm, presented in Figs. 10 and 11.

Weak pulses [blue curves in Figs. 12(b) and 12(c)] are absorbed in the droplet in the regime where absorption is not yet saturated, and therefore a relatively large fraction of their energy is absorbed. In contrast, for stronger pulses [orange and red curves in Figs. 12(b) and 12(c)], the absorption is saturated, and the absorbed energy represents a smaller fraction of the pulse energy. As a result, the energy ratios E_1/E_0 and E_2/E_0 are larger for stronger pulses.

The droplet-waveguide distance δ also strongly affects the Q-factors of the resonant WGM modes in the 2D droplet. We compute the eigenfrequencies and the corresponding Q-factors of the eigenmodes using the Harminv algorithm in the Meep software package, as described in Appendix A. Technically, we place a line source inside the droplet, which emits a short pulse of plane waves [placed on a line shifted away from the symmetry axis at $R - 4$ $\mu\mathrm{m} \le x \le R$ and $y = 0.2$ μm, with a polarization $\boldsymbol{E} = (1, 0, 1)$, central wavelength $\lambda_0 = 580$ nm, and spectral width $\mathrm{FWHM}_\lambda = 210$ nm], and then use the FDTD method to compute light propagation inside the droplet for 33 ps after the pulse has ended. During this time, we record the temporal evolution of the electric field components $E_z(t)$ and $E_y(t)$ at $x = 0$, $y = R - 0.1$ μm, and use Harminv to extract the eigenfrequencies and Q-factors of the TE and TM modes, respectively. The first-order resonant TE and TM WGMs are presented in Fig. 12(d) as a spectrum $Q(\lambda)$, where λ is the vacuum wavelength, for several values of δ and for a case without waveguides in the vicinity of the droplet. In the latter case, the Q-factors are highest; when the waveguides are brought closer,

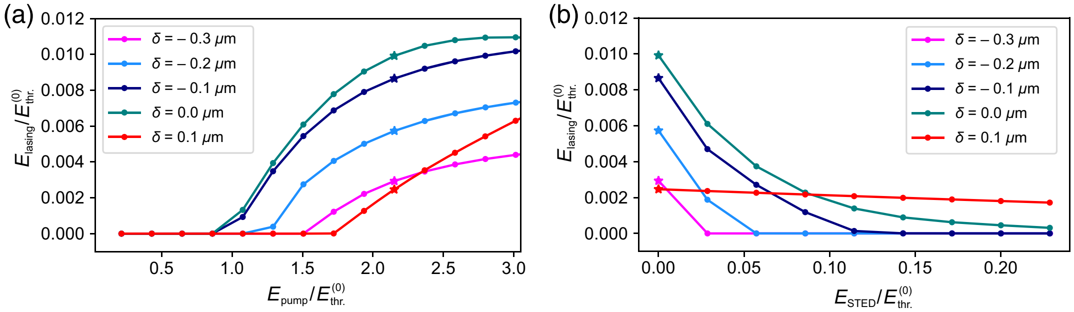

Fig. 13 (a) Lasing pulse energy as a function of pump pulse energy for several droplet-waveguide separations δ. Both energies are normalized to the lasing threshold pump pulse energy $E^{(0)}_{\text{thr.}}$ in the reference geometry with $\delta = -0.1\ \mu$m. (b) Lasing pulse energy as a function of STED pulse energy at a fixed pump pulse energy $E_{\text{pump}}/E^{(0)}_{\text{thr.}} = 2.152$, for different separations δ.

the WGM light couples out of the droplet into the waveguides more easily, which is reflected in a reduction of the Q-factors by several orders of magnitude.

By bringing the waveguides closer to the droplet (decreasing δ) more light is coupled into the droplet, which by itself lowers the lasing threshold, but at the same time it reduces the Q-factors, which results in the increase of the threshold. The actual outcome of the competition between these two effects is shown in Fig. 13(a), which plots the lasing pulse energy E_{lasing} as a function of the pump pulse energy E_{pump}. Both energies are normalized to the threshold pump pulse energy for lasing $E^{(0)}_{\text{thr.}}$ in the reference geometry with $\delta = -0.1\ \mu$m. A comparable, even slightly lower, lasing threshold than in the reference case is obtained for $\delta = 0\ \mu$m, whereas for $\delta = -0.2\ \mu$m and $\delta = -0.3\ \mu$m the thresholds are higher—presumably because of lower Q-factors. Besides that, the lasing threshold is also higher for $\delta = +0.1\ \mu$m; in that case, most probably due to the fact that only a small fraction of the pump light is coupled into the droplet.

Figure 13(b), analogous to Fig. 11(d), shows the lasing energy E_{lasing} as a function of the STED pulse energy E_{STED} at a fixed pump pulse energy $E_{\text{pump}}/E^{(0)}_{\text{thr.}} = 2.152$ and for several values of δ. Interestingly, for $\delta = 0.1$ the STED pulse that should suppress lasing couples into the droplet so weakly that the lasing energy decreases with increasing STED energy E_{STED} much more slowly than in the geometries with $\delta \leq 0\ \mu$m.

4 Discussion and Conclusion

Our work demonstrates a photonic device that is assembled in an aqueous environment, is made of soft matter, and uses a resonant concept to control light by light. There are several important conclusions to be drawn from the results. First, we have shown how an LC droplet in aqueous medium spontaneously forms an efficient optical contact with the polymer waveguide, which is, contrary to expectations, very robust and efficient. The stability and robustness of the polymer fibre-LC droplet contact are due to the balance of the surface tension that provides mutual attraction due to line tension forces. It would be difficult to achieve something like this in solids, clearly highlighting the advantage of soft matter over the solid matter for photonic interconnections. We could envisage that similar self-assembled photonic elements and coupled, multidroplet-cavity systems could be formed just by engineering surface properties and line tension of liquids and LCs in contact with polymers.

Second, we have demonstrated that LC droplets coupled to tapered polymer waveguides are an excellent photonic platform for future studies. The WGM lasing is achieved at very low pumping threshold fluences, which indicates very efficient excitation of dyed LC in the cavity-waveguide system.

We could envisage several interesting directions for future research. For example, nematic LCs doped with fluorescent dyes are known for their exceptionally high third order nonlinearities[33–36] and interesting optical phenomena could emerge along these studies in LC droplets. Indications of nonlinear Kerr optical effect are visible in the WGM lasing spectrum in Fig. 7(a) and STED in Fig. 8. Above the lasing threshold, one can clearly see that the lasing wavelengths are shifting to the blue end of the spectrum by increasing the pump light and lasing intensity. This could be explained by the increase of the index of refraction of the nematic liquid crystal, which is linear in the intensity of light that induces this nonlinear optical effect. The nearly linear dependence of the lasing wavelength shift with increasing pump fluence is more clearly seen in Fig. S6 in the Supplementary Material.

Furthermore, it is expected that optical cavities of more solid-like LC phases, such as the smectic-A phase, could exhibit even higher Q-factors because of their layered, solid-like structure that reduces order parameter fluctuations and enhances the surface tension. Optical cavities could be made of other exotic LC phases, such as various blue phases (BPs) that combine fluidity, crystallinity, chirality, and are topologically nontrivial. Lasing has already been reported from the bulk BP II liquid crystal,[37] which is a soft crystal made entirely of topological defects that are organized in striking 3D patterns, thus exhibiting band structure for light propagation. Droplets of BP I and II have been studied experimentally and theoretically,[38] and it has been demonstrated that topological defects and band structure can be controlled by droplet size, temperature, and surface anchoring. WGM in BP I and II droplets could show interesting spectral properties by combining band-gap properties and self-interference of light circulating in a BP droplet. Finally, the BP III phase of liquid crystal is a truly liquid, i.e., positionally and orientationally disordered, stable phase of topological defects,[39] which shows large optical rotation. A combination of optical rotation and self-interference of WGMs in a BP III droplet could lead to spectral properties, which may be of fundamental interest.

Third, and in our opinion the most important, we demonstrated a resonant concept of manipulating light by light by taking advantage of slow light and strong light-matter interaction in an optical cavity. The proposed STED resonant depletion of light by light in a cavity is based on energy manipulation, rather than changing material properties in intense light fields, utilizing the directionality of stimulated emission from a cavity. The energy stored upon the excitation of the cavity is always taken by the EM wave in a specific direction. Because this is a resonant process in an optical cavity, the efficiency of this process is greatly enhanced by the Q factor of the cavity. This is clearly seen from the energy, which is needed for efficient depletion in resonant versus nonresonant conditions. For example, in super-resolution microscopy, the STED pulse that depletes the electronic states of excited fluorescent molecules is typically three orders of magnitude stronger than the excitation pulse. This is because the STED photons make only a single pass through the sample and leave. However, in our WGM depletion experiments, the STED pulse is less than an order of magnitude stronger compared with the excitation pulse. This is more than hundred-fold reduction of the energy needed for efficient depletion of electronic states of the fluorescent molecules, and is clearly due to the multipass nature of STED photons in the cavity. By circulating inside the cavity by total reflection at the droplet's interface, STED light is continuously depleting the excited states; thereby efficiency of the STED process is expected to be enhanced by the Q-factor of the system.

In conclusion, we presented a self-assembled soft-matter micro-photonic element, a soft-matter photonic switch that uses concept of light-by-light manipulation at very low light intensity. As such, this is a rare example of a photonic device based on self-organizing properties of soft matter that could be a building block of a futuristic, bioinspired soft photonic platform.[40,41] This bio-inspired photonic platform would require less production energy compared to mainstream hard-matter photonic platforms, because soft matter is processed at lower temperatures. Furthermore, a soft-matter platform could drastically reduce the number of production steps, because soft matter has an important ability to self-organize. Finally, a soft-matter photonic platform could be made of environmentally friendly organic materials, which could reduce chemical waste, as soft-matter devices can be made both biodegradable and biocompatible.

5 Appendix A: Methodological Details

Light propagation is modeled using the finite-difference time-domain (FDTD) method[31] in the Meep software.[32] We propagate the electric and magnetic fields, $\mathbf{E}(\mathbf{r},t)$ and $\mathbf{H}(\mathbf{r},t)$, in space and time according to full Maxwell's equations and the geometry described by the dielectric tensor $\underline{\varepsilon}(\mathbf{r})$. The light propagation is modeled in a two-dimensional cross section of the actual structure (Fig. S7 in the Supplementary Material). In isotropic parts, the refractive index is n; in the liquid crystal, we have ordinary refractive index n_o and extraordinary index n_e, and the dielectric tensor is $\varepsilon_{ij} = n_o^2\delta_{ij} + (n_e^2 - n_o^2)n_i n_j$ with $i, j \in \{x, y, z\}$, where n_i and n_j are the components of the director field $\mathbf{n}(\mathbf{r}) = (n_x, n_y, n_z)$. The director field inside the droplet has a radial structure $\mathbf{n}(\mathbf{r}) = (\mathbf{r} - \mathbf{r}_0)/|\mathbf{r} - \mathbf{r}_0|$, where $\mathbf{r}_0 = (0\ \mu\text{m}, 5\ \mu\text{m})$; see Fig. S7 in the Supplementary Material. The structure is surrounded by perfectly matched layers (PMLs) of thickness 700 nm that fully absorb electromagnetic waves and provide open boundary conditions.

In water and in polymer waveguides, we assume no absorption. In the droplet we have an isotropic saturable dye on which light can get absorbed or amplified via stimulated emission. The dye is described by a four-level system [Fig. S7(b) in the Supplementary Material] that absorbs photons with energies equal to the energy difference between energy levels 1 and 4 and emits photons with energies equal to the energy difference between levels 2 and 3. Such a system is characterized by the absorption spectra in Fig. S6(c) in the Supplementary Material. Absorption and stimulated emission are also governed by the state of the dye, which is described by the fields of the occupations of energy levels $N_1(\mathbf{r},t)$, $N_2(\mathbf{r},t)$, $N_3(\mathbf{r},t)$, $N_4(\mathbf{r},t)$. The light absorption (index a) between energy levels 1 and 4, and amplification via stimulated emission (index e) between levels 2 and 3 are modeled via the classical oscillator model for polarization $\mathbf{P}_a$ and $\mathbf{P}_e$:[32]

$$\frac{\mathrm{d}^2\mathbf{P}_a(\mathbf{r},t)}{\mathrm{d}t^2} + \gamma_a\frac{\mathrm{d}\mathbf{P}_a(\mathbf{r},t)}{\mathrm{d}t} + \left(\omega_a^2 + \left(\frac{\gamma_a}{2}\right)^2\right)\mathbf{P}_a(\mathbf{r},t)$$
$$= -\Delta N_a(\mathbf{r},t)\sigma_a\mathbf{E}(\mathbf{r},t),$$

$$\frac{\mathrm{d}^2\mathbf{P}_e(\mathbf{r},t)}{\mathrm{d}t^2} + \gamma_e\frac{\mathrm{d}\mathbf{P}_e(\mathbf{r},t)}{\mathrm{d}t} + \left(\omega_e^2 + \left(\frac{\gamma_e}{2}\right)^2\right)\mathbf{P}_e(\mathbf{r},t)$$
$$= -\Delta N_e(\mathbf{r},t)\sigma_e\mathbf{E}(\mathbf{r},t),$$

where ω_a is the central frequency and γ_a is the frequency FWHM of the dye's absorption spectrum, ω_e is the central frequency and γ_e is the frequency FWHM of the emission spectrum, $\Delta N_a(\mathbf{r},t) = N_4(\mathbf{r},t) - N_1(\mathbf{r},t)$, $\Delta N_e(\mathbf{r},t) = N_3(\mathbf{r},t) - N_2(\mathbf{r},t)$, σ_a is the isotropic absorption cross-section, and σ_e is the isotropic stimulated emission cross-section. Time-dependent polarization is added to the electric field as $\mathbf{E}(\mathbf{r},t) = \mathbf{D}(\mathbf{r},t) - \mathbf{P}_a(\mathbf{r},t) - \mathbf{P}_e(\mathbf{r},t)$ at each time instance. The interaction between the dye and the light, together with non-radiative transitions from level 4 to level 3 with rate Γ_{43} and from level 2 to level 1 with rate Γ_{21}, results in the level populations change:

$$\frac{\partial N_1(\mathbf{r},t)}{\partial t} = +\Gamma_{21}N_2(\mathbf{r},t) - \frac{1}{\omega_a\hbar}\mathbf{E}(\mathbf{r},t)\cdot\left(\frac{\partial}{\partial t} + \frac{\gamma_a}{2}\right)\mathbf{P}_a(\mathbf{r},t),$$

$$\frac{\partial N_2(\mathbf{r},t)}{\partial t} = -\Gamma_{21}N_2(\mathbf{r},t) - \frac{1}{\omega_e\hbar}\mathbf{E}(\mathbf{r},t)\cdot\left(\frac{\partial}{\partial t} + \frac{\gamma_e}{2}\right)\mathbf{P}_e(\mathbf{r},t),$$

$$\frac{\partial N_3(\mathbf{r},t)}{\partial t} = +\Gamma_{43}N_4(\mathbf{r},t) + \frac{1}{\omega_e\hbar}\mathbf{E}(\mathbf{r},t)\cdot\left(\frac{\partial}{\partial t} + \frac{\gamma_e}{2}\right)\mathbf{P}_e(\mathbf{r},t),$$

$$\frac{\partial N_4(\mathbf{r},t)}{\partial t} = -\Gamma_{43}N_4(\mathbf{r},t) + \frac{1}{\omega_a\hbar}\mathbf{E}(\mathbf{r},t)\cdot\left(\frac{\partial}{\partial t} + \frac{\gamma_a}{2}\right)\mathbf{P}_a(\mathbf{r},t).$$

To reproduce the results from experiments, the following values of the parameters of the dye are used (in units $2\pi c_0/\mu\text{m}$): $\omega_a = 1/\lambda_a = 1/0.530$, $\omega_e = 1/\lambda_e = 1/0.570$, $\gamma_a = \gamma_e = 0.16$. This gives the absorption and emission spectra centered at 530 nm and 570 nm, respectively, with FWHM of ~50 nm; see Fig. S7(c) in the Supplementary Material.

Absorption and stimulated emission cross-sections are $\sigma_a = \sigma_e = 0.002$, and transition rates (in units $c_0/\mu\text{m}$) $\Gamma_{43} = 10$ and $\Gamma_{21} = 100$. At the beginning, the dye is in the ground state with $N_1(\mathbf{r}, t = 0) = 60$, $N_2(\mathbf{r}, t = 0) = 0$, $N_3(\mathbf{r}, t = 0) = 0$, $N_4(\mathbf{r}, t = 0) = 0$.

Both pump and STED pulses originate at the bottom of the right polymer waveguide, 1.4 μm from the edge of the simulation domain; see Fig. S7(a) in the Supplementary Material. Both pulses propagating along the y-axis have the shape of a Gaussian beam with focus at the source, waist size 1.5 μm, and linear polarization along x-axis. The pump pulse has a vacuum wavelength of 532 nm, and the STED pulse has a vacuum wavelength of 600 nm. The time-envelopes of both pulses have Gaussian profiles with FWHM of 1.57 ps (471 Meep units). The STED pulse is delayed by 4.67 ps (1400 Meep units) compared with the pump pulse. The amplitudes of the electric fields in Meep units at the source plane are set to $\sqrt{1500}$ for pump and 0 or $\sqrt{100}$ for STED pulses in Fig. 10. In Figs. 11(a) and 11(c), the amplitude of the pump is varied across values from $\{\sqrt{50}, \sqrt{100}, \dots, \sqrt{2100}\}$, while the amplitude of STED is 0. In Figs. 11(b) and 11(d), the amplitude of the pump is set to $\sqrt{1500}$, while the amplitude of STED is varied across values from $\{\sqrt{0}, \sqrt{5}, \dots, \sqrt{110}\}$. Lasing in simulations is triggered by a weak (electric field amplitude of 0.05), temporally short (0.008 ps), and thus spectrally broad (FWHM 85 nm) bidirectional seed sources of plane-wave electromagnetic radiation (radiating in $+x$ and $-x$ directions) with central vacuum wavelength of 570 nm. There are two seed sources that turn on and off every 0.83 ps. Odd pulses originate from the $x = -0.25$ μm plane and even pulses originate from the $x = +0.25$ μm plane. The size of the source plane along y-axis is $2.2\,R = 30.8$ μm. Both triggering sources are polarized along $\hat{\mathbf{E}}_0 = (0, 1, 1)$, to possibly initiate both TM and TE modes.

During the simulation, the intensity flux (surface integral of the Poynting vector) is accumulated at the bottom of the left waveguide, 1.4 μm from the edge of the simulation domain on the plane labelled as “Flux OUT” in Fig. S7(a) in the Supplementary Material. The accumulated spectrum of the intensity flux $\phi(\lambda)$ is calculated via Fourier transformation, as implemented in Meep software. We further introduce the total lasing energy as $E_{\text{lasing}} = \int_{567\text{ nm}}^{587\text{ nm}} \phi(\lambda)\mathrm{d}\lambda$. Energies of the incoming pump [Figs. 11(a) and 11(c)], $E_{\text{pump}} = \int_{529\text{ nm}}^{535\text{ nm}} \phi_{\text{ref}}(\lambda)\mathrm{d}\lambda$, and STED [Figs. 11(b) and 11(d)] pulses, $E_{\text{STED}} = \int_{597\text{ nm}}^{603\text{ nm}} \phi_{\text{ref}}(\lambda)\mathrm{d}\lambda$, are always measured in a separate parallel simulation in the geometry without the droplet, as shown in Fig. S7(d) in the Supplementary Material, where $\phi_{\text{ref}}(\lambda)$ is measured at the top of the waveguide. The eigenfrequencies and the corresponding Q-factors of the eigenmodes are calculated using the Harminv method in the Meep software package.

6 Appendix B: Supplementary Videos

Video S1: This video shows how an LC micro-droplet is injected using a precise micro-injector in between a polymer scaffold on glass, printed by DLW (mov, 1.62 MB [URL: https://doi.org/10.1117/1.AP.8.2.026009.s1]).

Video S2: The video shows laser printing of a set of four polymer pillars on glass. The pillars serve not only as mechanical scaffold that supports the LC droplet injected in between the pillars, but also act as an optical waveguide, transmitting the light into and out of the droplet (mov, 536 KB [URL: https://doi.org/10.1117/1.AP.8.2.026009.s2]).

Video S3: The video shows a focus scan of the LC droplet nested in between four polymer waveguides. The scan starts at the base of the waveguides (i.e., interface to glass supporting slide) and proceeds across the LC droplet. The image is captured between crossed polarizers (mov, 900 KB [URL: https://doi.org/10.1117/1.AP.8.2.026009.s3]).

Video S4: The video shows how an LC droplet, still attached to the micro-pipette of the injector, approaches a pillar-waveguide. A 532 nm light is sent through the waveguide but cannot be seen directly because it is blocked by an optical filter. When the droplet touches the pillar, it starts lasing the green WGM light (mov, 2.82 MB [URL: https://doi.org/10.1117/1.AP.8.2.026009.s4]).

Video S5: The video shows a high-magnification image of the contact area between an inflated LC drop (large circle on the right) and a DLW printed waveguide. The top of the waveguide is not visible because of the dark circular spot, which is a pinhole that collects light from the waveguide. Note the LC surface attraction to the waveguide and deformation of the spherical surface of the LC drop (mov, 4.94 MB [URL: https://doi.org/10.1117/1.AP.8.2.026009.s5]).

Video S6: The video shows how a dyed LC droplet nested in the scaffold of four polymer waveguides starts lasing when a 532 nm pumping light is sent through the upper-left waveguide and the intensity of this light is increased. The green light is due to WGM lasing; the 532 nm light is blocked by a filter (mov, 1.11 MB [URL: https://doi.org/10.1117/1.AP.8.2.026009.s6]).

Video S7: The video shows a focus scan of a lasing LC droplet in between the four polymer waveguides (mov, 688 KB [URL: https://doi.org/10.1117/1.AP.8.2.026009.s7]).

Video S8: The video shows numerical simulation of lasing (upper panel) and STED (lower panel) of WGM light from dyed LC droplet (mov, 2.34 MB [URL: https://doi.org/10.1117/1.AP.8.2.026009.s8]).

Video S9: The video shows an LC droplet in contact with a single pillar of elliptical shape with 20 and 5 μm semi-axis, respectively. The contact is strong enough to keep the droplet in place even after displacement by the micro-injector needle occurring at 12 s. After the displacement, the droplet returns to its starting position while remaining in contact with the pillar (MP4, 3.48 MB [URL: https://doi.org/10.1117/1.AP.8.2.026009.s9]).

Disclosures

All authors declare no competing interests.

Code and Data Availability

All data in support of the findings of this paper are available within the article or as Supplementary Material.

Acknowledgments

This project has received funding from the European Research Council (ERC) under the European Union’s Horizon 2020 Research and Innovation Program (Grant No. 884928-LOGOS). MR and IM acknowledge financial support from Slovenian Research and Innovation Agency (ARIS) (Grant No. P1-0099).

References

1. M. Kolle and S. Lee, "Progress and opportunities in soft photonics and biologically inspired optics," *Adv. Mater.* **30**, 1702669 (2018).
2. E. Yablonovitch and T. J. Gmitter, "Photonic band structure: the face-centred-cubic case," *Phys. Rev. Lett.* **63**, 1950–1953 (1989).
3. A. R. Parker, "515 million years of structural colour," *J. Opt. A: Pure Appl. Opt.* **2**, R15 (2000).
4. P. Vukusic, J. R. Sambles, and C. R. Lawrence, "Colour mixing in wing scales of a butterfly," *Nature* **404**, 457 (2000).
5. M. Kolle, "Photonic structures inspired by nature," PhD Thesis, University of Cambridge (2010).
6. M. Scalora et al., "Optical limiting and switching of ultrashort pulses in nonlinear photonic band gap materials," *Phys. Rev. Lett.* **73**, 1368 (1994).
7. R. Soref and B. Bennett, "Electrooptical effects in silicon," *IEEE J. Quantum Electron.* **23**, 123–129 (1978).
8. V. R. Almeida et al., "All-optical control of light on a silicon chip," *Nature* **431**, 1081–1084 (2004).
9. J. Leuthold, C. Koos, and W. Freude, "Nonlinear silicon photonics," *Nat. Photonics* **4**, 535–544 (2010).
10. K. J. A. Ooi et al., "All-optical control on a graphene-on-silicon waveguide modulator," *Sci. Rep.* **7**, 12748 (2017).
11. C. Koos et al., "All-optical high-speed signal processing with silicon–organic hybrid slot waveguides," *Nat. Photonics* **3**, 216–219 (2009).
12. X. Hu et al., "All-optical switching of defect mode in two-dimensional nonlinear organic photonic crystals," *Appl. Phys. Lett.* **87**, 231111 (2005).
13. R. Katouf et al., "Ultra-fast optical switches using 1D polymeric photonic crystals," *Photonics Nanostruct. – Fundam. Appl.* **3**, 116–119 (2005).
14. X. Hu et al., "Picosecond and low-power all-optical switching based on an organic photonic-bandgap microcavity," *Nat. Photonics* **2**, 185–189 (2008).
15. S. W. Hell and J. Wichmann, "Breaking the diffraction resolution limit by stimulated emission: stimulated-emission-depletion fluorescence microscopy," *Opt. Lett.* **19**, 780–782 (1994).
16. M. Vitek and I. Muševič, "Nanosecond control and optical pulse-shaping by stimulated emission depletion in a liquid crystal," *Opt. Express* **23**, 16921–16932 (2015).
17. M. Vellaichamy et al., "Microscale generation and control of nanosecond light by light in a liquid crystal," *Nat. Photonics* **19**, 758–766 (2025).
18. M. Humar et al. "Electrically tunable liquid crystal optical microresonators," *Nat. Photonics* **3**, 595–600 (2009).
19. K. J. Vahala, "Optical microcavities," *Nature* **424**, 839–846 (2003).
20. M. Saito, H. Shimatani, and H. Naruhashi, "Tunable whispering gallery mode emission from a microdroplet in elastomer," *Opt. Express* **16**, 11915–11919 (2008).
21. D. K. Cohoon, "An exact solution of Mie type for scattering by a multilayer anisotropic sphere," *J. Electromagn. Wave* **3**, 421–448 (1989).
22. A. Matsko and V. Ilchenko, "Optical resonators with whispering-gallery modes-part I: basics," *IEEE J. Sel. Top. Quantum. Electron.* **12**, 3–14 (2006).
23. M. Deubel et al., "Direct laser writing of three-dimensional photonic-crystal templates for telecommunications," *Nat. Mater.* **3**, 444–447 (2004).
24. S. Nocentini et al., "Three- dimensional photonic circuits in rigid and soft polymers tunable by light," *ACS Photonics* **5**, 3222–3230 (2018).
25. Z. He et al., "Novel liquid crystal photonic devices enabled by two-photon polymerization," *Opt. Express* **27**, 11472–11491 (2019).
26. J. S. O'Neill et al., "3D switchable diffractive optical elements fabricated with two-photon polymerization," *Adv. Opt. Mat.* **10**, 2102446 (2022).
27. A. Martinez et al., "Mutually tangled colloidal knots and induced defect loops in nematic fields," *Nat. Mater.* **13**, 258–263 (2014).
28. S. Nocentini et al., "Structured optical materials controlled by light," *Adv. Opt. Mater.* **6**, 1800167 (2018).
29. S. M. Morris et al., "Correlations between the performance characteristics of a liquid crystal laser and the macroscopic material properties," *Phys. Rev. E* **74**, 061709 (2006).
30. T. V. Truong, L. Xu, and Y. R. Shen, "Early dynamics of guest-host interaction in dye-doped liquid crystalline materials," *Phys. Rev. Lett.* **90**, 193902 (2003).
31. A. Taflove, A. Oskooi, and S.G. Johnson, *Advances in FDTD Computational Electrodynamics: Photonics and Nanotechnology*, Artech, Norwood, MA (2013).
32. A. Oskooi et al. "MEEP: a flexible free-software package for electromagnetic simulations by the FDTD method," *Comput. Phys. Commun.* **181**, 687–702 (2010).
33. I. Jánossy, A. D. Lloyd, and B. S. Wherrett, "Anomalous optical Freedericksz transition in an absorbing liquid crystal," *Mol. Cryst. Liq. Cryst. Incorpor. Nonlinear Opt.* **179**, 1–12 (1990).
34. I. Jánossy, L. Csillag, and A. D. Lloyd, "Temperature dependence of the optical Fréedericksz transition in dyed nematic liquid crystals," *Phys. Rev. A* **44**, 8410–8413 (1991).
35. L. Marrucci and D. Paparo, "Photoinduced molecular reorientation of absorbing liquid crystals," *Phys. Rev. E* **56**, 1765–1772 (1997).
36. T. V. Truong, L. Xu, and Y. R. Shen, "Dynamics of the guest-host orientational interaction in dye-doped liquid-crystalline materials," *Phys. Rev. E* **72**, 051709 (2005).
37. W. Cao et al., "Lasing in a three-dimensional photonic crystal of the liquid crystal blue phase II," *Nat. Mater.* **1**, 111–113 (2002).
38. J. A. Martínez-Gonzáleza et al., "Blue-phase liquid crystal droplets," *Proc. Natl. Acad. Sci.* **112**, 13195–13200 (2015).
39. J. Pišljar, S. Ghosh, and S. Turlapati, "Blue phase III: topological fluid of skyrmions," *Phys. Rev. X* **12**, 011003 (2022).
40. I. Muševič, "Integrated and topological liquid crystal photonics," *Liq. Cryst.* **41**, 418–429 (2014).
41. L.-L. Ma et al., "Self-assembled liquid crystal architectures for soft matter photonics," *Light: Sci. Appl.* **11**, 270 (2022).

Vandna Sharma received her PhD in physics from Chitkara University, Punjab, India, in 2020. She completed her postdoctoral research in soft-matter photonics at the Jozef Stefan Institute, Ljubljana (Slovenia). Currently, she is an assistant professor at Chitkara University, Punjab, India. Her research interests include liquid crystal droplets, liquid crystal-based display devices, and advanced electro-optical soft materials with nanomaterials for next-generation photonic technologies.

Jaka Zaplotnik is a PhD student and researcher at the faculty of Mathematics and Physics, University of Ljubljana, and at the Jožef Stefan Institute. His work focuses on computational photonics and soft matter physics, with an emphasis on liquid crystals and light–matter interactions. He applies numerical methods and machine learning techniques to model, simulate, and optimize complex physical systems in photonic soft-matter research.

Maruša Mur received her BSc, MSc, and PhD degrees in physics from the University of Ljubljana, Slovenia, in 2011, 2013, and 2019, respectively. The main topic of her PhD thesis was photonics of liquid crystal dispersions. Currently, she is a postdoctoral researcher at the Jožef Stefan Institute, Ljubljana, Slovenia, where she works on bio-integrated photonics, recently on 3D printing inside living cells.

Jaka Pišljar received his PhD from the Faculty of Mathematics and Physics, University of Ljubljana, Slovenia, in 2023. He is currently a postdoctoral researcher at the Condensed Matter Physics Department of the Jožef Stefan Institute in Ljubljana, Slovenia. His research focuses on soft-matter photonics and topological phenomena in liquid crystals, including blue phases and half-skyrmion systems.

Uroš Jagodič received his PhD in physics from the Jožef Stefan Postgraduate School in 2019. He is a physicist specialized in soft-matter photonics and liquid-crystal physics. He develops three-dimensional microstructures using direct laser writing, focusing on structured liquid-crystal alignment, micro-photonics, and microfluidic systems. His research interests include programmable light–matter interaction, topological soft-matter platforms, and optically active colloidal architectures.

Andreja Jelen obtained her PhD from the Faculty of Natural Sciences and Engineering, University of Ljubljana. She completed postdoctoral fellowship at the Korea Basic Sciences Institute in Daejeon, Republic of Korea. Her current research interest is exotic correlative electron microscopy techniques utilization (SEM, FIB and TEM) for diverse physical phenomena explorations and practical applications.

Miha Škarabot obtained his master's and PhD degrees in physics from the University of Ljubljana. He is an associate professor of physics at the University of Ljubljana and a Senior Scientist at the Jožef Stefan Institute. He is an experimental physicist, and his main research interests include liquid crystals, especially colloids, defects, and surfaces.

Urban Mur is a postdoctoral researcher at the Faculty of Mathematics and Physics, University of Ljubljana. He received his PhD in physics from the University of Ljubljana in 2021 and was a postdoctoral researcher at the University of Oxford from January 2024 to December 2025. His research focuses on numerical modelling of light–matter interactions in soft and anisotropic materials, particularly liquid crystals and photonic and meta-photonic structures, using finite-difference computational methods.

Miha Ravnik is head of the Soft Matter Physics Group, head of the Physics Department, and vice-dean at the Faculty of Mathematics and Physics, University of Ljubljana, as well as a research councillor at the Jožef Stefan Institute. His expertise lies in modelling and theory of soft matter and complex systems. His research interests include complex fluids, active matter, colloids, liquid crystals, optical and photonic anisotropic media, topological materials, and protein biophysics.

Igor Muševič is a professor of physics at the University of Ljubljana, as well as a research councillor and head of the Soft Matter Laboratory, which he established in 1995, at the Jožef Stefan Institute. He received his BSc and PhD degrees in physics from the University of Ljubljana. He is a soft-matter experimental physicist, and his recent research topics include liquid crystal colloids, phase transitions in liquid crystals, and experimental topology and photonics of soft matter.